# Untangling microfibres: Pervasive plastic pollution in submarine canyons

This is a non peer-reviewed preprint submitted to EarthArXiv.

Currently in review with the Journal of the Geologic Society London

**Ed Keavney[1], Ian A. Kane[2], Michael A. Clare[3], David M. Hodgson[1], Veerle A.I. Huvenne[3], Esther J. Sumner[4], Jeff Peakall[1], Furu Mienis[5], and Jonathan Kranenburg[5]**

[1] *School of Earth and Environment, University of Leeds, Leeds, LS2 9JT, UK*

[2] *Department of Earth and Environmental Science, University of Manchester, Manchester, M13 9Pl, UK*

[3] *Ocean BioGeoscience, National Oceanography Centre, Southampton, SO14 3ZH, UK*

[4] *School of Ocean and Earth Science, University of Southampton, Southampton, SO14 3ZH, UK*

[5] *Department of Ocean Systems, Royal Netherlands Institute for Sea Research (NIOZ-Texel), Den Burg, The Netherlands*

Corresponding author: Ed Keavney (ed.keavney@gmail.com)

## ABSTRACT

Submarine canyons are important conduits for microplastic transport to the deep sea via turbidity currents. However, other near-bed oceanographic flows and sub-seafloor processes may play an important role in the transport and burial of microplastics. We use sediment push-cores for microplastic and sediment grain-size analysis from two transects across the Whittard Canyon, UK, to show that complex process-interactions control the transport and burial of microplastics and semi-synthetic microfibres in the thalweg and on the canyon flanks. Microplastic pollution is pervasive across the canyon at both transects, from the thalweg and from 500 m higher on the flanks, despite turbidity currents being confined to the canyon thalweg. Furthermore, we calculate sediment accumulation rates from $^{210}$Pb dating and show that microplastic concentrations remain similar at sediment depths down to 10 cm. This reveals that the huge global-increase in plastic production rates over time is not recorded, and that microplastics are present in sediments that pre-

date the mass-production of plastic. The interaction of turbidity currents, deep-tidally-driven currents, and sub-seafloor processes shreds any potential signal that microplastics may provide as indicators of historical plastic production rates, which undermines the utility of microplastics as reliable markers of the onset of the Anthropocene.

## 1. Introduction

Plastic production increased 700%, from 50 million tonnes (Mt) in the 1970's to >400 Mt in 2022 (PlasticsEurope, 2023). More than 10 Mt of plastic enters the world ocean annually (Lebreton *et al*., 2017). Microplastics (<1 mm diameter particles) represent ~13.5% of the marine plastic budget (Koelmans *et al*., 2017), including primary (manufactured particles; Zitko and Hanlon, 1991) and secondary (derived from the breakdown of macroplastics; Andrady, 2011) microplastics. Semi-synthetic microfibres (*e.g.,* composed of rayon and chlorinated rubber) are equally persistent in the natural environment (Athey and Erdle, 2022; Finnegan *et al*., 2022), are observed in deep-sea sediments (Woodall *et al*., 2014), and have similar detrimental effects on biota (Jiang *et al*., 2024) as plastic microfibres. Semi-synthetic microfibres are commonly used in clothes manufacturing (*e.g.,* Napper and Thompson, 2016) and cigarette filters (*e.g.,* Belzagui *et al*., 2021). Therefore, we use 'microfibre' to encompass synthetic and semi-synthetic microfibres, and 'anthropogenic microparticles' to encompass both microplastic particles and microfibres.

Lacustrine and shallow-marine settings act as archives to calculate the rate and quantity of pollutant delivery (such as anthropogenic microparticles) and allow monitoring of how stresses on ecosystems have changed over time (Brandon *et al*., 2019; Uddin *et al*., 2021 and references therein). Few studies have acquired sedimentary time-series records of anthropogenic microparticles in the deep sea (*e.g.,* Chen *et al*., 2020), despite being the ultimate sink for plastics

(Thompson *et al*., 2004; Woodall *et al*., 2014; Koelmans *et al*., 2017; Choy *et al*., 2019). Furthermore, none exist in submarine canyons, which host important seafloor ecosystems (Treigner *et al*., 2006; Fernandez-Arcaya *et al*., 2017), and are the main conduits for delivering particulate matter (Normark, 1970; Talling *et al*., 2023), including pollutants (Paull *et al.*, 2002; Zhong and Peng, 2021; Pierdomenico *et al*., 2023), from terrestrial and coastal settings to the deep sea. Avalanches of sediment, known as turbidity currents, flow through submarine canyons and are responsible for generating Earth's largest sediment accumulations (Curray and Moore, 1971). These flows are thought to be the main agent for anthropogenic microparticle transfer to, and sequestration on, the deep seafloor (Kane and Clare, 2019; Pohl *et al*., 2020; Rohais *et al*., 2024; Zhang *et al*., 2024), yet other hydrodynamic processes can affect anthropogenic microparticle concentrations (Kane *et al*., 2020). It is increasingly recognised that processes other than turbidity currents control particulate transport and burial in submarine canyons (*e.g.*, Maier *et al*., 2019; Bailey *et al*., 2024; Hage *et al*., 2024; Palanques *et al*., 2024), and it is possible that we have underestimated the importance of other hydrodynamic and sub-seafloor processes and anthropogenic activities. However, the role of hydrodynamic and sub-seafloor processes, and human activities on anthropogenic microparticle dispersal in submarine canyons remains unconstrained. This uncertainty results from a lack of targeted seafloor sampling and sedimentological context, therefore limiting our understanding of anthropogenic microparticle fluxes to the deep sea, threats to deep-seafloor ecosystems, and deep-sea anthropogenic sedimentary archives.

Our aim is to determine the interplay of anthropogenic microparticle transport and burial processes in the deep-sea using a dataset from the Whittard Canyon. We assess these processes by integrating detailed seafloor observations from multibeam bathymetric mapping and video footage acquired from a Remotely Operated Vehicle (ROV), with analysis of 4 box-cores to quantify sediment accumulation rates and 9 push-cores to quantify the sediment grain-size and anthropogenic microparticle concentration in surficial seafloor sediments. To meet this aim, the following objective are addressed: i) to map the distribution and concentration of anthropogenic microparticles throughout the Whittard Canyon, ii) to document changes in anthropogenic microparticle concentration with burial depth, iii) to assess sediment grain-size trends associated with the anthropogenic microparticle distribution and concentration, and integrate the findings with sediment accumulation rates, and iv) to discuss how anthropogenic microparticle transport and burial processes controls their transfer in submarine canyons.

## 2. Setting and methods

### 2.1. Whittard Canyon

The head of Whittard Canyon lies at ~200 m water depth in the Celtic Sea, ~300 km from the nearest coast (Fig. 1A). Four main branches incise steeply into the shelf break. The canon extends oceanward for ~150 km, to ~3800 m water depth (Amaro *et al.*, 2016). The upper-reach of the Eastern Branch extends ~55 km, from the head to ~2960 m water depth, with steep canyon flanks and a >2° thalweg slope, with a vertical relief from flank to thalweg of ~1000 m (Fig. 1B, C and E). The lower-canyon reach extends to ~3800 m water depth, with lower gradient canyon flanks and a <2° thalweg slope, with a vertical relief from flank to thalweg of ~1250 m (Fig. 1B, C and E). Further details of the canyon’s geomorphology are included in the Supplemental Material.

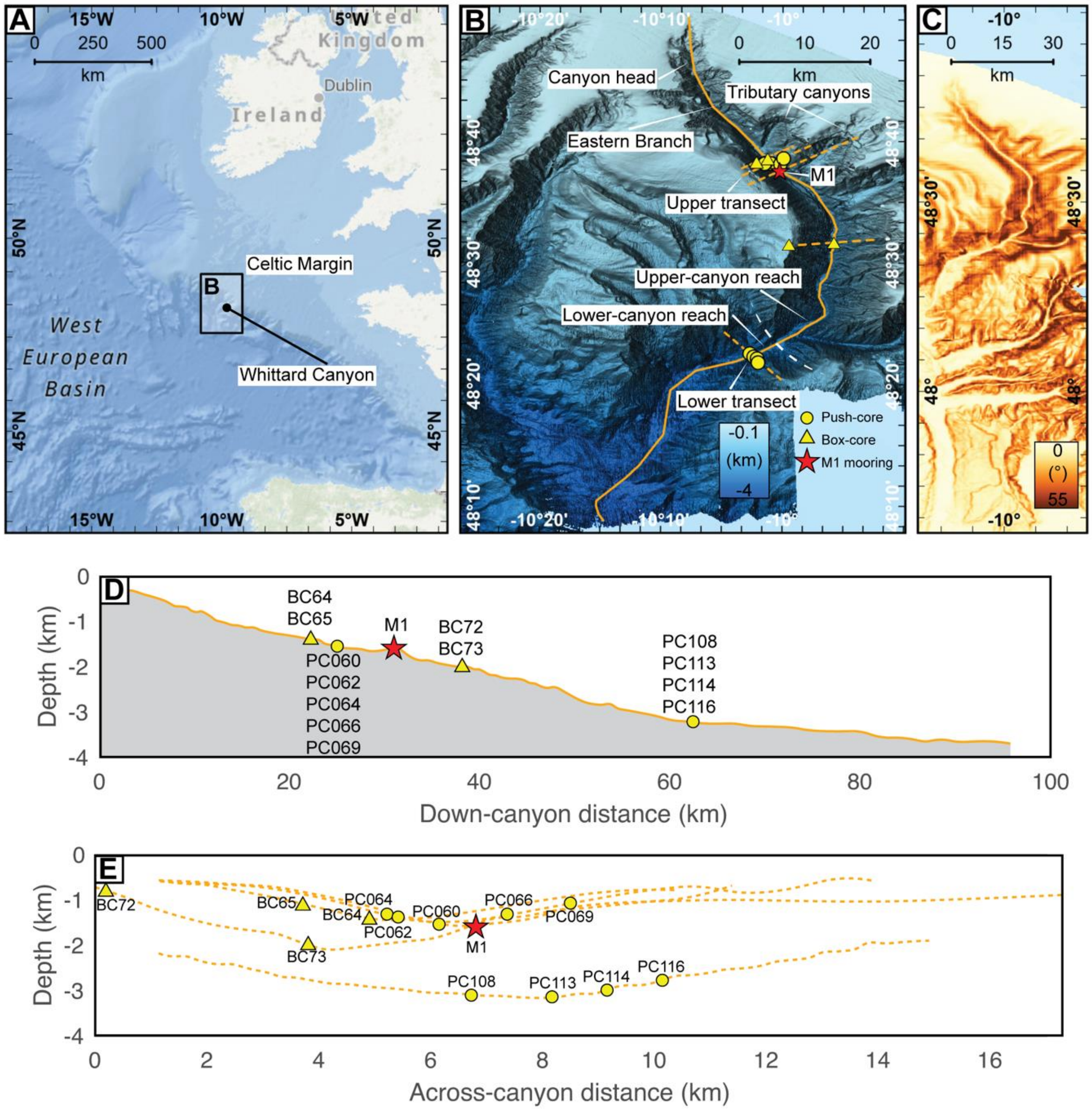


Fig. 1. Location of data used in this study. (A) Location of Whittard Canyon. (B) Location of the cores and hydrodynamic mooring in the Eastern Branch of Whittard Canyon. (C) Slope angle map of the Eastern Branch. (D) Longitudinal profile of the canyon thalweg. (E) Cross-sections through each transect (locations on B).

## 2.2. Fishing activity on the Celtic Margin

Fishing activities that disturb the seafloor (*i.e.*, benthic trawling) are common around the head of Whittard Canyon, and on many of its interfluves (Fig. 2). This trawling activity is a source of marine pollutants (Xue *et al*., 2020) and causes sediment resuspension (Daly *et al*., 2018). The cumulative annual benthic trawling effort for 2013-2014 and 2023-2024 was exported from GlobalFishingWatch (2024) for an area of 16,650 $km^2$ (48° - 49° N to 9° - 11° W) around the continental shelf, and Whittard Canyon (Fig. 2A and B). The trawling effort for the same period for the 661 $km^2$ (48° 10’ 2.56” - 48° 29’ 59.74” N to 9° 33’ 34.59” - 9° 47’ 52.25” W) area covered by The Canyons Marine Conservation Zone was also exported (Fig. 2C and D). The Marine Conservation Zone was designated in October 2013, following the identification of vulnerable ecosystems, including burrowing megafauna and cold-water corals (Duineveld *et al*., 2001). The intensity of benthic trawling on the Celtic Margin has increased fivefold in the ten-year period from 2013-2014 to 2023-2024 (GlobalFishingWatch, 2024; Fig. 2).

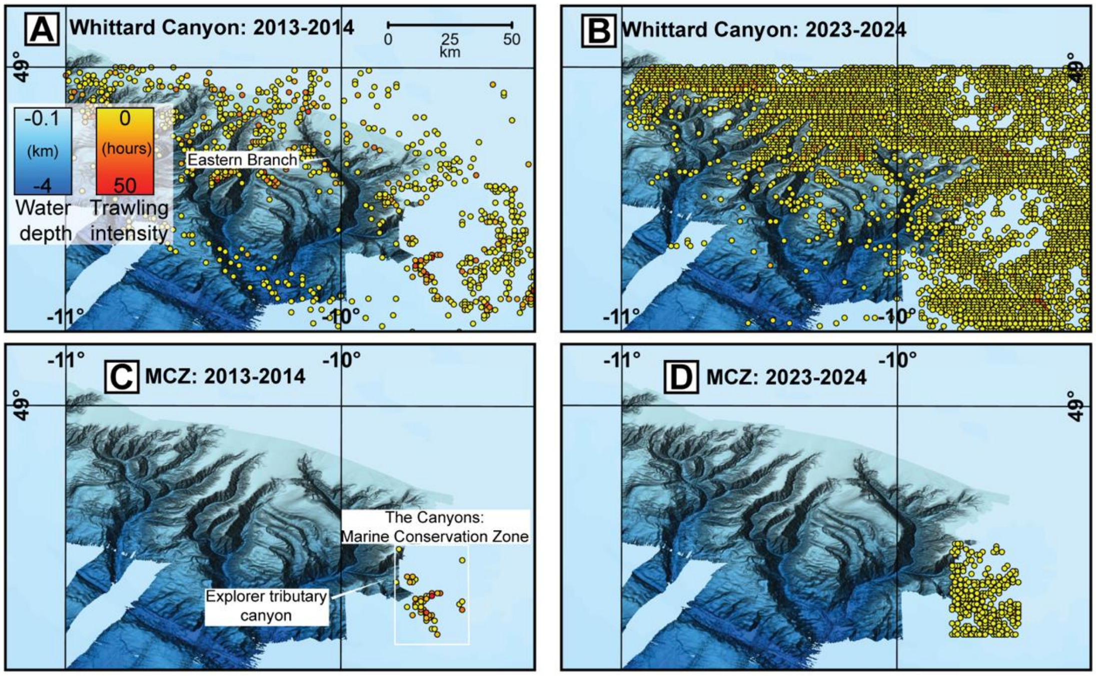


Fig. 2. Intensity of benthic trawling as recorded by Global Fishing Watch. (A) the Whittard Canyon 2013-2014. (B) the Whittard Canyon 2023-2024. (C) Marine Conservation Zone (MCZ) 2013-2014. (D) Marine Conservation Zone (2023-2024).

### 2.3. Hydrodynamic mooring

A moored, downward-looking, 600 kHz Acoustic Doppler Current Profiler (M1 mooring – Fig. 1B: 30 m above seafloor; 1500 m water depth) in the Eastern Branch recorded near-bed hydrodynamic conditions from June 2019 – June 2020, including vigorous (up to 1 $ms^{-1}$) internal tides and 6 turbidity currents. These turbidity currents had maximum down-canyon velocities of 1.5-5.0 $ms^{-1}$, flow thicknesses >30 m, and accumulated quartz-rich, fine sand in a sediment trap 10 m above seafloor (Heijnen *et al*., 2022; Fig. 3A). The frequency and velocity of the turbidity currents recorded by the ADCP during the sampling period document how the Whittard Canyon experiences turbidity current activity analogous in frequency and velocity to many land-attached canyons, despite being land-detached (Heijnen *et al.*, 2022).

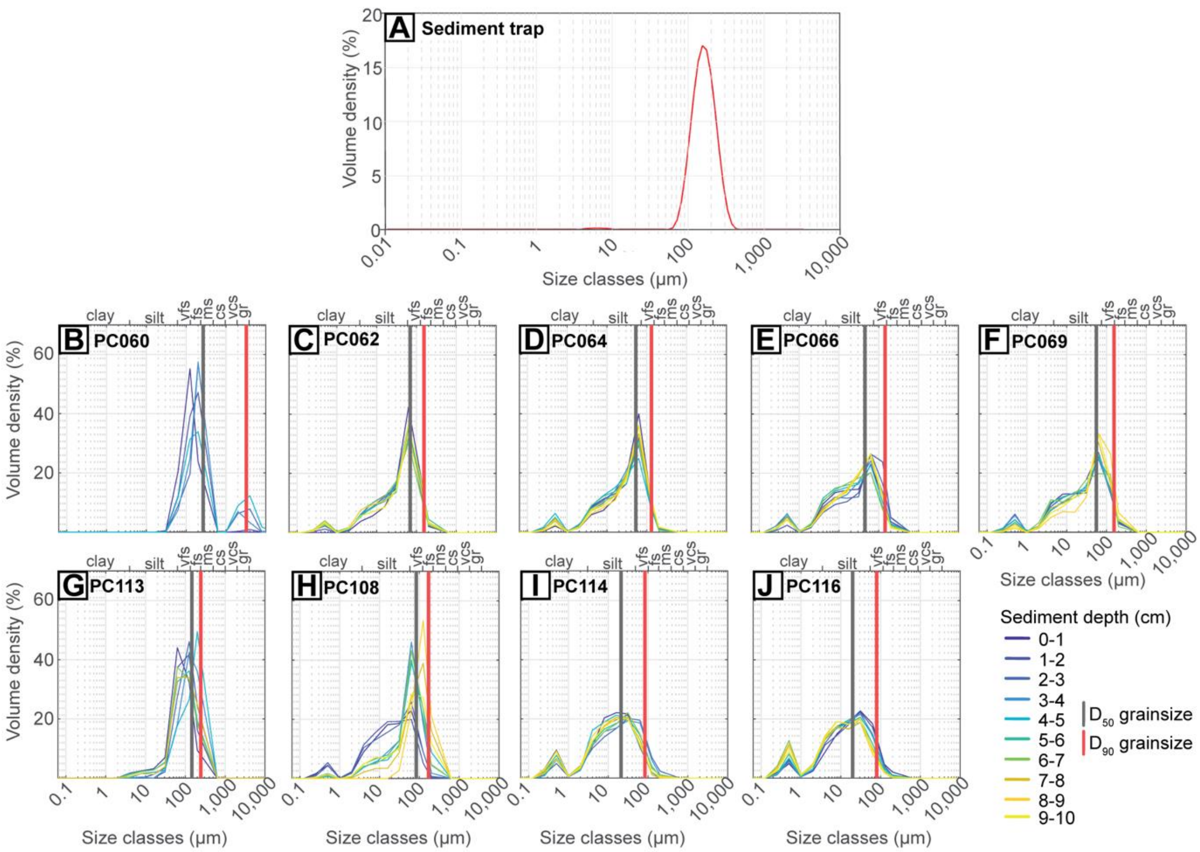


Fig. 3. Grain-size distribution plots. (A) The sediment trap at the M1 mooring site of Heijnen *et al*. (2022). (B-J) The push-cores of the current study.

### 2.4. Sediment push-core recovery

Five precisely-located push-cores were collected using the ROV 'ISIS', along an across-canyon transect in the upper-canyon reach (24.9 km from the head, 1062-1546 m water depth) from 34 metres above thalweg (m.a.t.) to 521 m.a.t. on the canyon flank. Four precisely-located push-cores were also collected from an across-canyon transect in the lower-canyon reach (62.3 km from the head, 2773-3204 m water depth) (Fig. 1B, D and E) from 0 m.a.t. to 431 m.a.t. on the canyon flank. The push-cores were recovered from the upper-transect on the 21st August 2022, and from the lower-transect on the 2nd September 2022. All 9 push-cores were subsampled at 1 cm depth-intervals, down to 10 cm, depending on core recovery (subsample n=83), for anthropogenic microparticle extraction, and sediment grain-size analysis (Table S1). High-resolution bathymetric data enable investigation of the effects of submarine canyon geomorphology on anthropogenic microparticle distribution

## 2.5. Laboratory procedures

### *2.5.1. Anthropogenic microparticle extraction, identification, and quantification*

The 1 cm sediment core horizons had variable weights and water content, so samples were dried overnight in a drying oven set to 50˚C. The dried samples were weighed, and for comparative purposes the weight and anthropogenic microparticle content were normalised to 50 g dry sediment weight. Sediment samples were then stored in glass beakers covered with aluminum foil. Samples were added to a 1 L glass beaker with ~700 mL of a dense $ZnCl_2$ solution (1.6 g $cm^{-3}$) and disaggregated using a magnetic stirrer, and mixed until homogenized. The microplastics were extracted from the sediment using a Sediment Microplastic Isolation (SMI) unit following a protocol developed for microplastic extraction (Coppock *et al*., 2017) and modified following Nel *et al*. (2019). The solution was added to the SMI unit, and the beaker was rinsed with $ZnCl_2$ solution to flush any remaining sediment/anthropogenic microparticles. Prior to each use, the SMI unit was disassembled and thoroughly rinsed with Class 1 Milli-Q de-ionized water. Following settling overnight, the headspace supernatant was isolated by closing the ball valve of the SMI unit and rinsing with extra $ZnCl_2$ solution to flush any remaining anthropogenic microparticles before vacuum filtering over a Whatman 541, 22 $\mu$m filter paper. The prepared filter paper was then placed in a labelled petri dish and covered. Throughout the extraction procedure, all individuals wore white cotton laboratory coats and latex gloves. All the extraction stages were performed in a clean laboratory in a fume cupboard. When the sediment samples were mixing in the 1 L beaker, and settling in the SMI units they were covered with aluminum foil to limit airborne anthropogenic microparticle contamination. When it was not possible during the sample preparation to cover the sediment sample with aluminum foil, an opened petri dish with a blank, Whatman 541, 22 $\mu$m, filter paper was placed in the fume cupboard and used as a contamination control procedural blank. When the prepared filter paper was exposed during the anthropogenic microparticle identification stage, a second contamination control procedural blank was also collected, again using an opened petri dish with a blank, Whatman 541, 22$\mu$m, filter paper, placed in the microscopy laboratory (Table S2).

The prepared filter papers, both from the extraction process and the airborne contamination control blanks were analysed in a clean microscopy laboratory using a Zeiss Axio Zoom, V16 stereomicroscope at 20-50X magnification. Here, we define anthropogenic microparticles as between in 1 $\mu$m and 1 mm in size; the same size range used by prominent microplastic studies (*e.g.*, Browne *et al*., 2011; Claessens *et al*., 2011; Van Cauwenberghe *et al*., 2013, 2015; Vianello *et al*., 2013; Dekiff *et al*., 2014; Kane and Clare, 2019; Kane *et al*., 2020). Filter papers were traversed systematically to identify anthropogenic microparticles based on the following criteria: (i) no visible cellular or organic structures; (ii) a positive reaction to the hot needle test (de Witte *et al*., 2014); and (iii) maintenance of structural integrity when touched or moved. Anthropogenic microparticles were categorised based on their color and type, including, whether they were microfibres, microplastic fragments (including films), or microbeads (Table S1).

#### *2.5.2. Fourier Transform Infrared Spectroscopy*

Anthropogenic microparticles were visually identified using optical microscopy and a subset of particles were analysed using Fourier transform infrared (FTIR) spectroscopy for polymer confirmation. Identification of polymer composition was conducted on a subsample (n=13) of the extracted microplastics using a PerkinElmer Spotlight 400 FTIR spectrometer using transmittance mode (Fig. 4; Table S3). Further details are included in the Supplemental Material.

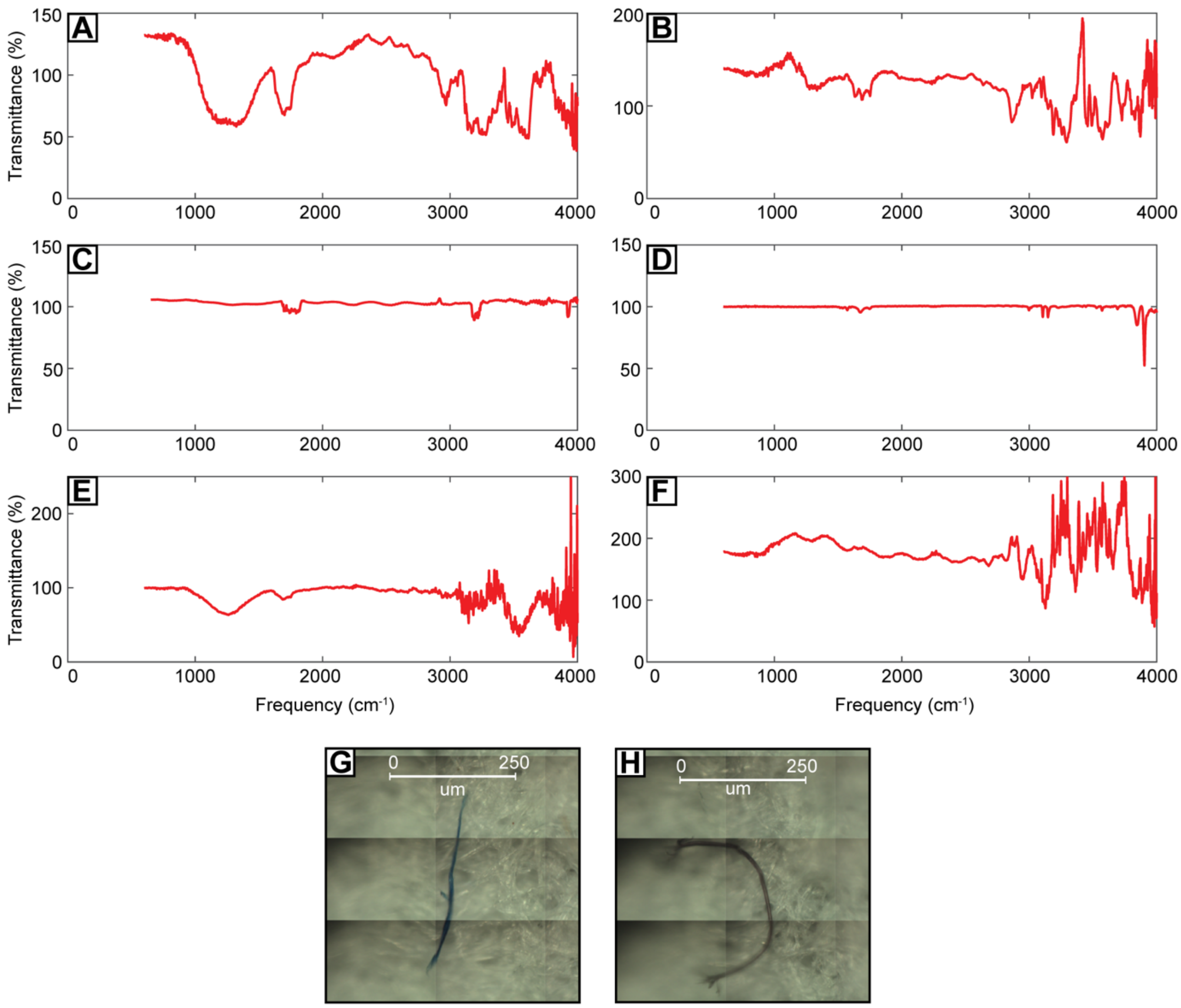


Fig. 4. Fourier transform infrared (FTIR) spectroscopy spectra and microscope photographs of microfibres. (A) Rayon FTIR spectra. (B) Polyester FTIR spectra. (C) Polyethylene FTIR spectra. (D) Polystyrene FTIR spectra. (E) Chlorinated rubber FTIR spectra. (F) Polypropylene FTIR spectra. (G) Photograph of polyester microfibre. (H) Photograph of rayon microfibre.

### *2.5.3. Grain-size analysis*

The grain-size of 79 of the 83 push-core samples was analysed using a Microtrac FLOWSYNC particle sizer (Microtrac MRB). The grain-size of the four remaining samples (PC060B-E) was analysed using the dry sieving method due to the FLOWSYNC particle sizer having an upper particle limit of 2000 $\mu$m, and the fragmented shell material in the samples exceeded this upper limit. The FLOWSYNC particle sizer uses tri-laser diffraction to measure particle size distribution with a lower particle limit size of 0.01 $\mu$m. The samples were subjected to a small amount of ultrasonic dispersion. Three aliquots were analysed to ensure that each sample was completely dispersed. The grain-size distribution, indicating the volume percentage of grains in a certain size interval, was constructed (Fig. 3B-J). The grain-size percentiles were exported from the FLOWSYNC software and are documented in Table S1.

#### ***2.5.4. $^{210}$Pb sediment accumulation rates***

Sediment accumulation rates derived from $^{210}$Pb dating of box-cores were recorded at 4 positions within the upper-canyon reach; 2 in the thalweg and 2 on the canyon flanks (Fig 5; Table S4). Sediment accumulation rates are calculated from the four box-cores (BC64, BC65, BC72, and BC73) (Fig. 5E-H; Table S4), using $^{210}$Pb dating. The box-cores were collected during the research cruise 64PE421 conducted by NIOZ (the Royal Netherlands Institute for Sea Research) from the 14$^{th}$ May 2017 – 25$^{th}$ May 2017. The recovery rate of the box-cores varied by location. Further details are included in the Supplemental Material.

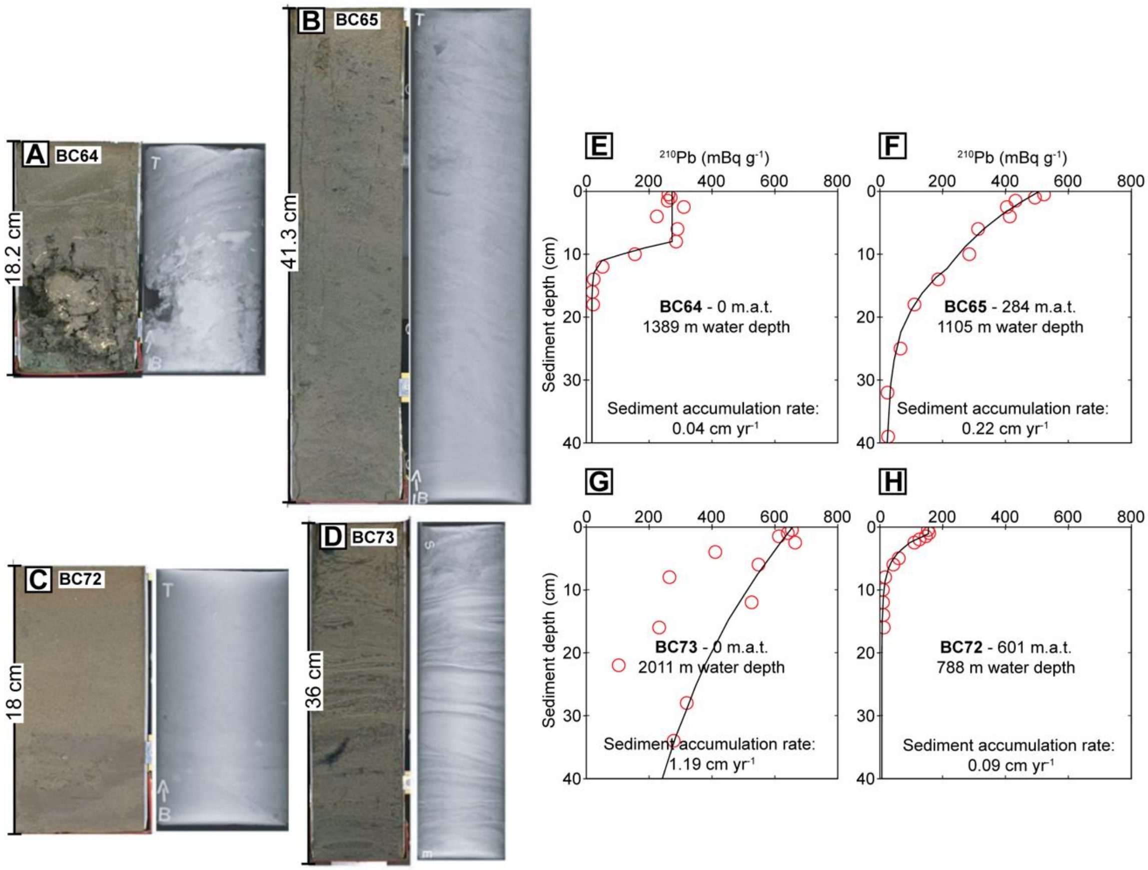


Fig. 5. (A-D) Core photographs and X-ray scans of the box-cores used in $^{210}$Pb dating. (E-H) the sediment accumulation rate plots for the box-cores. (A and E) Box-core 64. (B and F) Box-core 65. (C and G) Box-core 72. (D and H) Box-core 73. m.a.t. is meters above thalweg.

## 3. Results

### 3.1. Anthropogenic microparticle pollution in surficial sediments

Anthropogenic microparticles were present throughout all 9 push-cores (Figs. 6, 7C and 7F). A total of 1255 anthropogenic microparticles were observed with optical microscopy and a subset of the particles (n = 13) was verified with FTIR spectroscopy. Microfibres were the dominant anthropogenic microparticle type (microfibres = 91.3%, fragments = 5.7%, microbeads = 3.0%).

Herein, the anthropogenic microparticle count quantifies as the number of particles per 50 g of dry sediment weight (particles/50 g). FTIR spectroscopy confirms 62% of the anthropogenic microparticles are plastic, with common polymers including polyvinyl butyral, polyvinylchloride, and acrylic. The remaining 38% comprise semi-synthetic polymers, including chlorinated rubber and rayon (Fig. 4 ; Table S3).

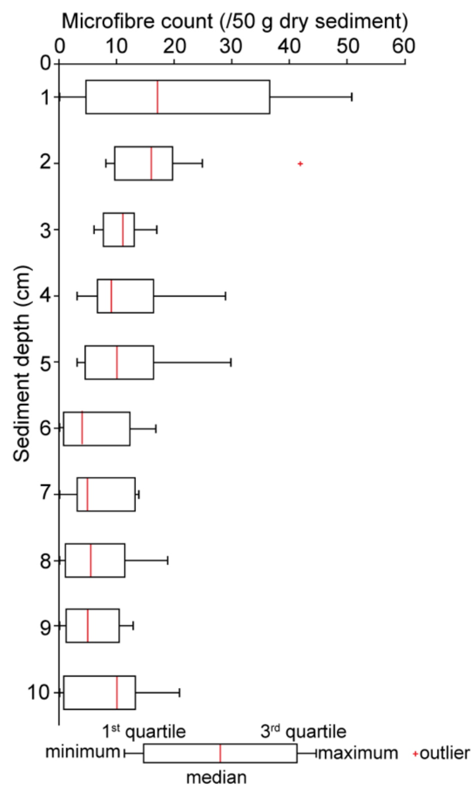


Fig. 6. Box plot for microfibre concentration and sediment depth for all push-cores.

### 3.2. Microfibres in the canyon thalweg

In push-core 060 (PC060) (34 m.a.t., at the upper-transect), the grain-size range is 31-8000 $\mu$m, and the arithmetic mean gravel% and sand% are 9.6% and 90.3%, respectively; the granule-sized particles are fragmented shells (Fig. 3B; Table S1). Microfibre count in PC060 increases with sediment depth from 4 to 30 microfibres/50 g (Fig. 7C). In PC113 (0 m.a.t. at the lower-transect), the grain-size range is 2-200 $\mu$m, and the arithmetic mean sand% and silt% are 92.4% and 7.6%, respectively (Fig. 3G; Table S1). Microfibre count in PC113 decreases by 62.5% with sediment depth (Fig. 7F).

The sediment accumulation rates in BC64 (1389 m water depth, 0 m.a.t.) and BC73 (2011 m water depth, 0 m.a.t.) are 0.04 cm $yr^{-1}$ and 1.19 cm $yr^{-1}$, respectively (Fig. 5E and G). Therefore, it could take 8.4-to-250 years to accumulate 10 cm of sediment in the canyon thalweg, meaning sediments containing anthropogenic microparticles in the thalweg may pre-date the mass production of plastic in the 1950's. The mobility of sediment within the thalweg can be observed in a photograph captured by the ROV ISIS during the recovery of PC060; a high level of suspended sediment is recorded in the water column of the thalweg following the passing of a turbidity current down-canyon (Fig. 8A).

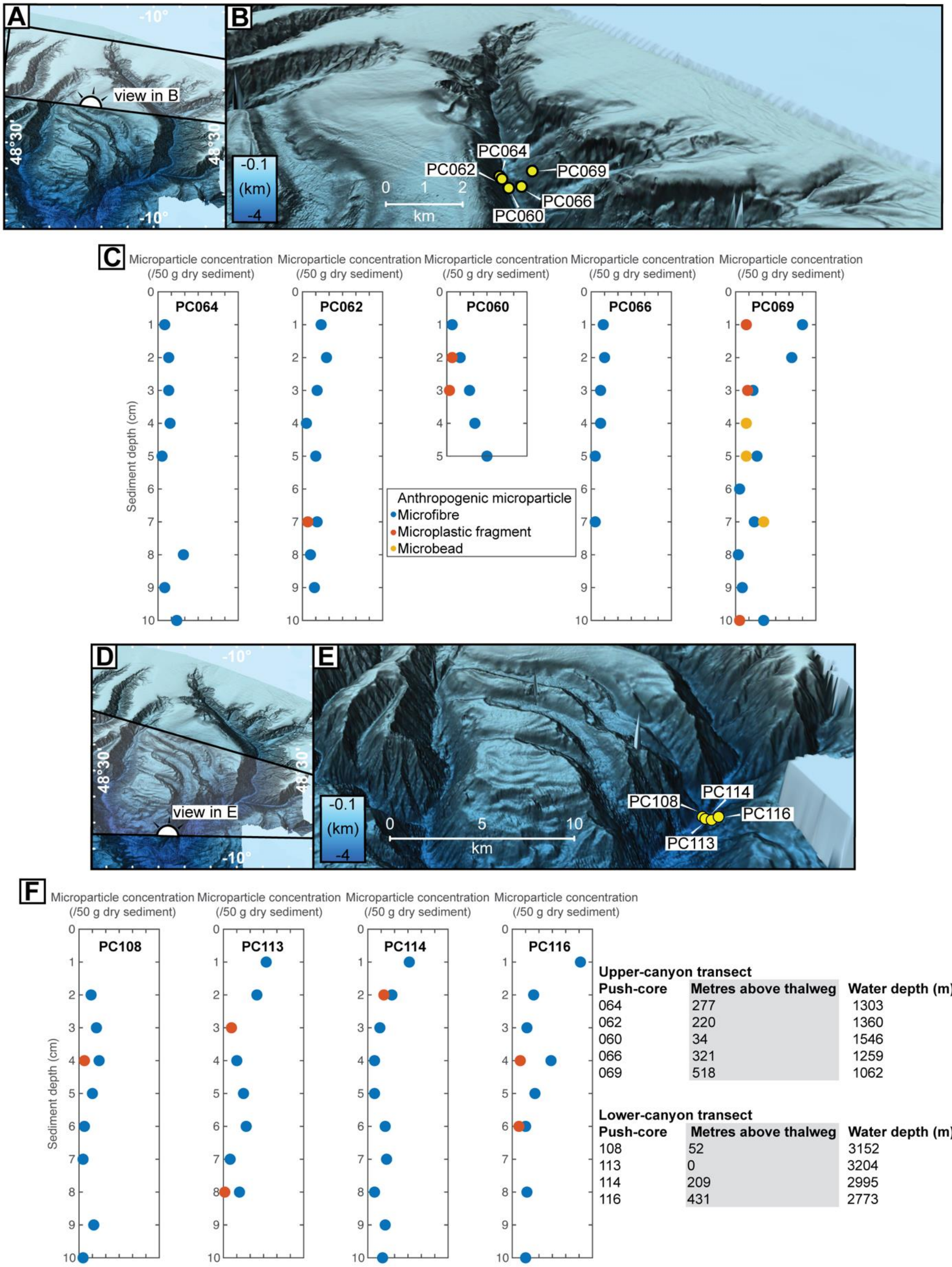
A
-10°
view in B
48°30'
48°30'
-10°
B
-0.1
(km)
-4
0 1 2
km
PC064
PC062
PC069
PC066
PC060
C
Microparticle concentration (/50 g dry sediment)
Sediment depth (cm)
PC064
PC062
PC060
PC066
PC069
Anthropogenic microparticle
Microfibre
Microplastic fragment
Microbead
D
-10°
48°30'
48°30'
view in E
-10°
E
-0.1
(km)
-4
0 5 10
km
PC108
PC114
PC116
PC113
F
Microparticle concentration (/50 g dry sediment)
Sediment depth (cm)
PC108
PC113
PC114
PC116
Upper-canyon transect
Push-core Metres above thalweg Water depth (m)
064 277 1303
062 220 1360
060 34 1546
066 321 1259
069 518 1062
Lower-canyon transect
Push-core Metres above thalweg Water depth (m)
108 52 3152
113 0 3204
114 209 2995
116 431 2773

Fig. 7. Anthropogenic microparticle count with sediment depth for the push-cores located in Whittard Canyon. (A, B, D, and E) Location maps and high-resolution bathymetric maps of the Eastern Branch. 3X vertical exaggeration. (C and F) Anthropogenic microparticle trends for each push-core.

### 3.3. Microfibres on the canyon flanks

At the upper transect, push-cores (PC062, PC064, and PC066, located 220, 277, and 321 m.a.t., respectively) have a grain-size range of 0.25-200 $\mu$m (clay-to-fine sand) (Fig. 3C, D and E), and an arithmetic mean sand% of 54.9%, 43.8%, and 39.9%, respectively (Table S1). Microfibre count in these cores is low and uniform, ranging from 0-19/50 g with an arithmetic mean of 7/50 g (Fig. 7C). PC069 (518 m.a.t.) is located near the tributary canyons at the upper transect; the grain-size range is also 0.25-200 $\mu$m, yet despite its increased height above the thalweg, the arithmetic mean sand% is 47.6% (Fig. 3F; Table S1). PC069 contains the greatest range of anthropogenic microparticle types, and an arithmetic mean microfibre count of 18/50 g (Fig. 7C; Table S1). At the lower transect, PC114 and PC116, located 209 and 431 m.a.t., respectively, have the same grain-size range as the canyon flank push-cores at the upper transect, but with an arithmetic mean sand% of 17.2% and 16.5%, respectively (Fig. 3I and J; Table S1). In these push-cores, the microfibre count decreases with depth by 64.5% and 80.3%, respectively (Fig. 7F and Table S1).

The sediment accumulation rates in BC65 (1105 m water depth, 284 m.a.t.) and BC72 (788 m water depth, 601 m.a.t.) are 0.22 cm $yr^{-1}$ and 0.09 cm $yr^{-1}$, respectively (Fig. 5F and H). Therefore, it could take 45-to-111 years to accumulate 10 cm of sediment on the canyon flanks and means that sediment containing anthropogenic microparticles on the canyon flanks may pre-date the mass-production of plastic.

On the canyon flanks at the upper transect, 277 m.a.t., and thus above the known thickness of the turbidity currents recorded by Heijnen *et al*. (2022), the crest orientation of sub-parallel ripples observed on the seafloor suggests a flow direction approximately perpendicular to the direction of turbidity current transport (Fig. 8B). This suggests that other hydrodynamic processes capable of sediment transport are also active on the canyon flanks (*e.g.*, internal tides).

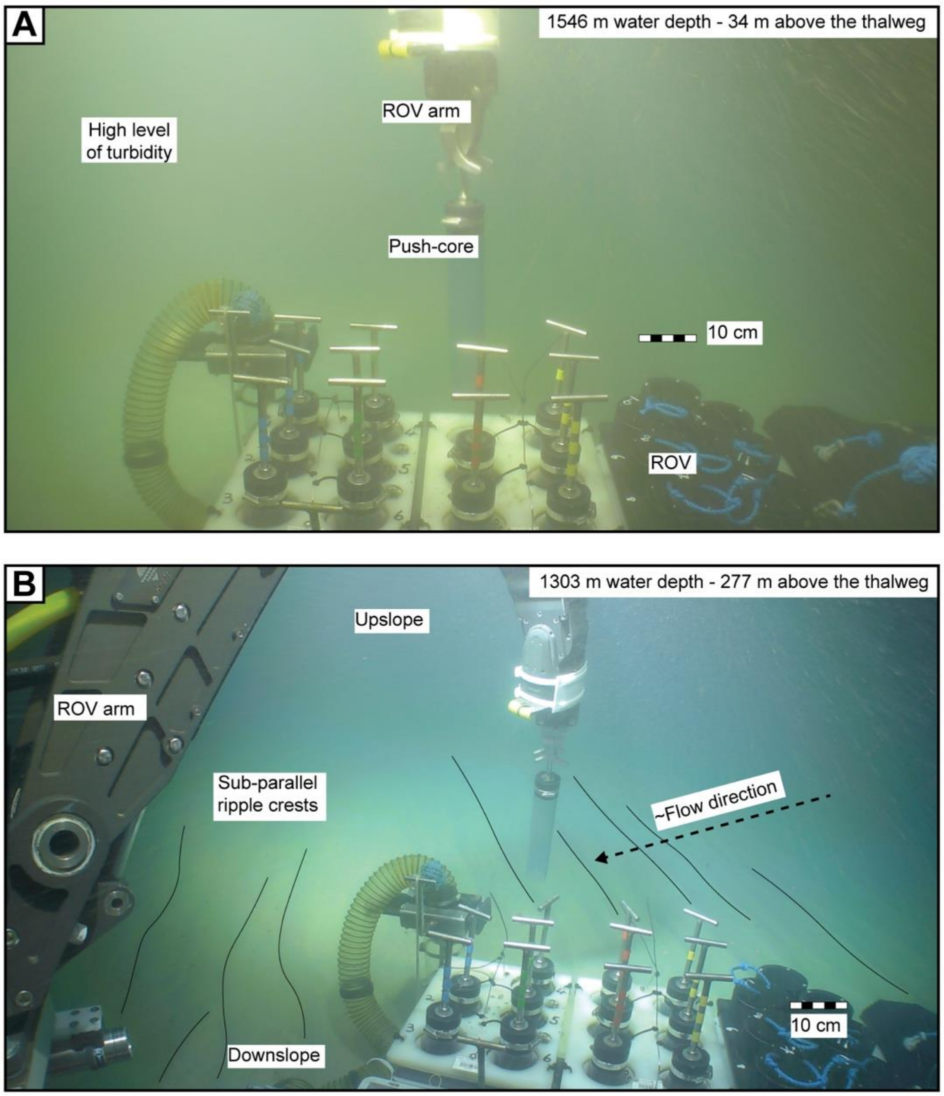


Fig. 8. Photographs taken of seabed push-core sampling from the Remotely Operated Vehicle. (A) Canyon thalweg at the upper-transect. (B) Canyon flanks at the upper-transect.

## 4. Discussion

### 4.1. Microfibre transport and burial processes

Microfibre pollution is pervasive throughout the Eastern Branch down to the 10 cm sediment depth of the push cores. Almost all push-cores show a gradual decline in microfibre concentration with depth. This gradual decline with depth is despite the marked differences in sediment accumulation rates across the canyon, and the 700% increase in the background plastic production rate. Microfibres are hypothesised to be transported to the canyon head via cross-continental shelf currents (Fig. 9A), and via vertical settling from marine sources (Fig. 9B and F), but their subsequent redistribution and burial cannot solely be explained by deposition from turbidity currents.

From the observed grain-size trends in the canyon thalweg (notably the absence of sediment <31 $\mu$m in PC060) we infer that the frequent (sub-annual) and fast (up to 5 $ms^{-1}$) turbidity currents serve to bypass and winnow silt-sized sediment and microfibres further down-canyon. However, microfibres were recorded at elevations up to 518 m.a.t., over an order of magnitude above the recorded thickness of measured turbidity currents. This suggests that other processes are important in the Whittard Canyon, and may need be considered in other submarine canyons (Fig. 9). The presence of sand in the canyon flank push-cores, and increased sand% 518 m.a.t., suggests that sediment is not sourced exclusively from hemipelagic fallout. The canyon flank sands point to sediment, and microfibres and other anthropogenic microparticles, stored on the Celtic Margin being transported via episodic turbidity currents in the tributary canyons or by sediment resuspension by benthic trawling close to the canyon head and on the canyon interfluves (Figs. 2, 3F, and 9; Table S1). Internal tides break against the steep topography of the canyon flanks in the upper-canyon and are focused into the canyon thalweg (Amaro *et al*., 2016; Hall *et al*., 2017; van

Haren *et al*., 2022), thus providing another mechanism for resuspending sediment and microfibres throughout the canyon (Fig. 9D). The location of BC72 (Fig. 1D and E), high on the canyon flank opposite the Celtic Margin and the tributary canyons, could help to explain the low sediment accumulation rates (Fig. 5F).

The observed uniformity of the gradual decline in microfibre concentration with sediment depth suggests, however, that sub-seafloor processes also affect microfibre burial processes in the deep sea. Hyporheic transfer of microplastics has been demonstrated in riverbeds (Frei *et al*., 2019). In sub-seafloor settings, hyporheic transfer is driven by pressure gradients, as exist between the base of turbidity currents and the seafloor (*e.g.*, Eggenhuisen and McCaffrey, 2012) and is invoked here as a control on the stratigraphic distribution of microfibres (Fig. 9E). Furthermore, sediment resuspension via internal tidal pumping (*e.g*., Li *et al*., 2019; Normandeau *et al*., 2024) on the canyon flanks may generate a sufficient pressure gradient to drive hyporheic transfer of microfibres through sediment pore spaces, where turbidity currents are not active. Microplastic infiltration depth increases positively with sediment grain-size (Waldschläger and Schüttrumpf, 2020), hence hyporheic transfer may be enhanced in the canyon thalweg compared to the canyon flanks (Fig. 9E).

Bioturbation may also play a role in controlling the vertical distribution of mirofibres in the sub-seafloor (Fig. 9E). The uppermost 10 cm of BC64 and BC65 are bioturbated (Fig. 5A and B). Sediment and microplastic mixing by bioturbation has been documented experimentally (Näkki *et al*., 2017) and is hypothesised to occur in deep-sea sediments (Courtene-Jones *et al*., 2020). The depth of the bioturbated layer extends to 10 cm in modern marine sediments, with individual burrows extending deeper (Tarhan *et al*., 2015) and may be enhanced on the canyon flanks, due to less stressed conditions for organisms to colonize compared to the thalweg (Fig. 9E).

Bioturbation and hyporheic transfer are likely important in transferring anthropogenic microparticles into pre-1950's deep-sea sediments; the latter supported in lakes where bioturbation is absent (Dimante-Deimantovica *et al*., 2024).

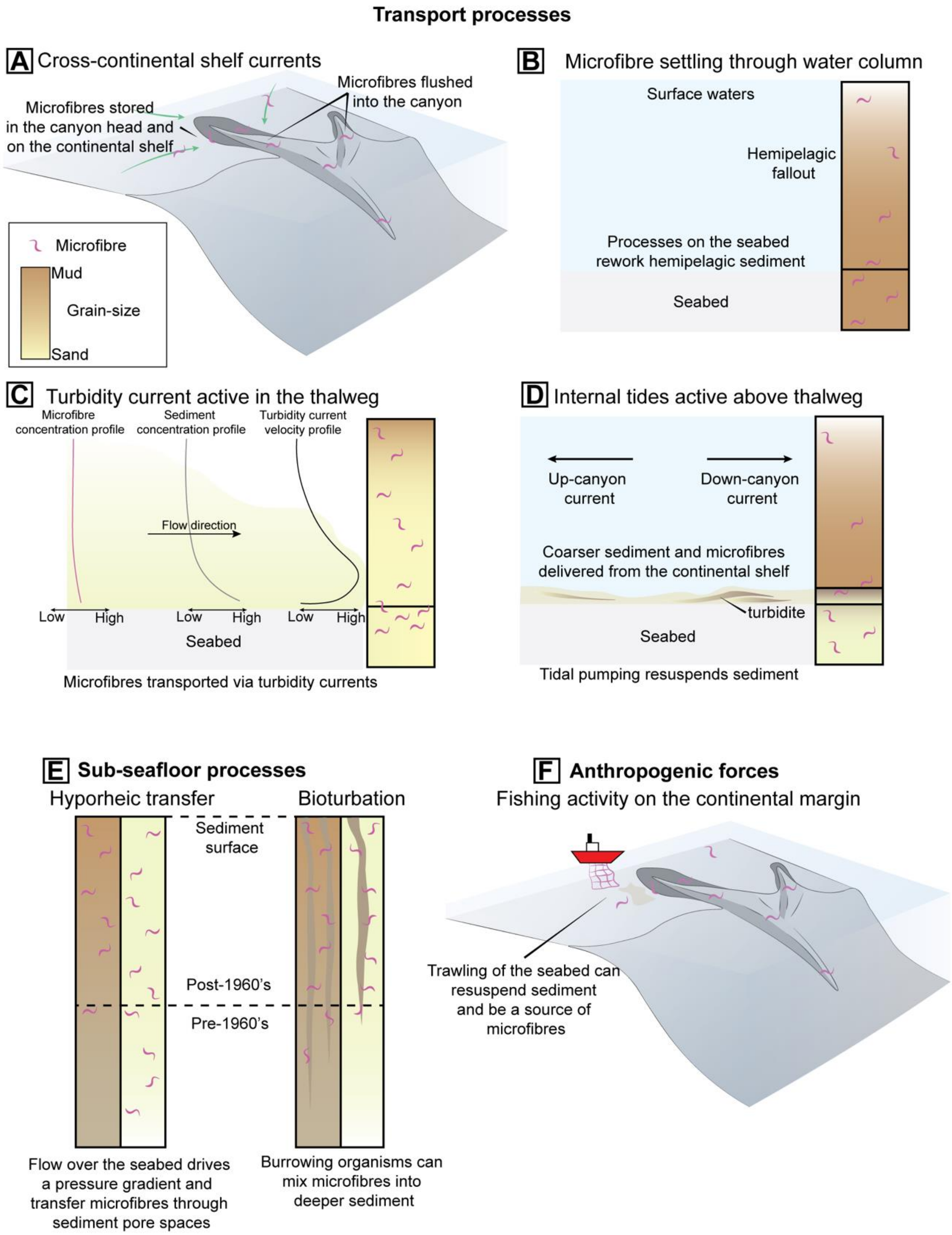


Fig. 9. Synthesis of microfiber transport and burial processes in submarine canyons. (A-D) Transport processes. (E) Sub-seafloor processes. (F) Anthropogenic forces.

## 4.2. Shredding of anthropogenic microparticle signals in the deep-sea

We suggest that sediment transport and burial processes, and anthropogenic forcing, act as nonlinear filters that shred the environmental signal of increasing plastic production rates through time in submarine canyons. The efficiency of anthropogenic microparticle transfer from land-based sources to the Whittard Canyon is relatively low, given the land-detached nature of the canyon. This suggests that anthropogenic microparticle pollution in land-detached canyons, of which there are >5000 (Harris and Whiteway, 2011), is dominantly marine-sourced, and that such systems receive a buffered supply of terrestrially-sourced anthropogenic microparticles. Given the dynamism of submarine canyons, the buffered supply of anthropogenic microparticles to land-detached canyons, and the mobility of microfibres and thus other anthropogenic microparticles in the sub-seafloor, the efficacy of using anthropogenic microparticles as anthropogenic tracer particles is questionable, along with calculations of their fluxes.

# 5. Conclusions

Our results show that anthropogenic microparticle pollution is pervasive in Whittard Canyon, to 10 cm sediment depth in both the thalweg, and on canyon flanks over 500 hundred meters above the thalweg. While turbidity currents are a major agent in the transfer of anthropogenic microparticles, the turbidity currents in Whittard Canyon are only 10s of meters thick (Heijnen *et al.*, 2022), suggesting other processes and sources of anthropogenic microparticles are important. Additional sources include hemipelagic settling, and sediments on the continental shelf resuspended by benthic trawling and entering tributary canyons. Transport and resuspension of anthropogenic microparticles by internal tidal pumping likely occurs across the entire canyon water depth. Almost all the push-cores show a gradual decline in anthropogenic microparticle concentrations down to 10 cm, despite the 700% increase in global plastic production since the 1970's. Where low sedimentation accumulation rates are recorded, much of the sediment in box-cores pre-dates plastic production. This suggests mobility of anthropogenic microparticles in the sub-seafloor, with likely processes including bioturbation and hyporheic transfer. The observed distribution of anthropogenic microparticles in Whittard Canyon demonstrates they are not entirely flushed through canyons, but may be permanently or transiently stored, and be mobile within the sediment bed. These results suggest that anthropogenic microparticles incorporated in deep-sea sediments may be a poor record of canyon particulate flux and that identifying the Anthropocene boundary using anthropogenic microparticles in these sediments may not be straightforward.

**CRediT author contribution statement**

**Ed Keavney:** Conceptualisation, Methodology, Formal analysis, Investigation, Writing – Original Draft, Visualisation. **Ian A. Kane:** Conceptualisation, Methodology, Resources, Writing – Review & Editing, Supervision, Project administration, Funding acquisition. **Michael A. Clare:** Conceptualisation, Resources, Writing – Review & Editing, Supervision, Project administration, Funding acquisition. **David M. Hodgson:** Conceptualisation, Writing – Review & Editing, Supervision, Project administration. **Veerle A.I. Huvenne:** Investigation, Writing – Review & Editing, Project Administration, Funding acquisition. **Esther J. Sumner:** Investigation, Writing – Review & Editing. **Jeff Peakall:** Conceptualisation, Writing – Review & Editing, Supervision. **Furu Mienis:** Investigation, Project administration, Funding acquisition. **Jonathan Kranenburg:** Methodology, Formal analysis, Visualisation.

**Acknowledgements**

We thank the Captain and crew of RSS James Cook cruise 38. This cruise was supported by the UK National Environmental Research Council (NERC) National Capability Programme (NE/R015953/1) "Climate Linked Atlantic Sector Science". H. Brown of the University of Leeds, and T. Bishop and J. Yarwood of the University of Manchester are thanked for help with analyses.

**Figure captions**

Fig. 1. Location of data used in this study. (A) Location of Whittard Canyon. (B) Location of the cores and hydrodynamic mooring in the Eastern Branch of Whittard Canyon. (C) Slope angle map of the Eastern Branch. (D) Longitudinal profile of the canyon thalweg. (E) Cross-sections through each transect (locations on B).

Fig. 2. Intensity of benthic trawling as recorded by Global Fishing Watch. (A) the Whittard Canyon 2013-2014. (B) the Whittard Canyon 2023-2024. (C) Marine Conservation Zone (MCZ) 2013-2014. (D) Marine Conservation Zone (2023-2024).

Fig. 3. Grain-size distribution plots. (A) The sediment trap at the M1 mooring site of Heijnen *et al*. (2022). (B-J) The push-cores of the current study.

Fig. 4. Fourier transform infrared (FTIR) spectroscopy spectra and microscope photographs of microfibres. (A) Rayon FTIR spectra. (B) Polyester FTIR spectra. (C) Polyethylene FTIR spectra. (D) Polystyrene FTIR spectra. (E) Chlorinated rubber FTIR spectra. (F) Polypropylene FTIR spectra. (G) Photograph of polyester microfibre. (H) Photograph of rayon microfibre.

Fig. 5. (A-D) Core photographs and X-ray scans of the box-cores used in $^{210}$Pb dating. (E-H) the sediment accumulation rate plots for the box-cores. (A and E) Box-core 64. (B and F) Box-core 65. (C and G) Box-core 72. (D and H) Box-core 73. m.a.t. is meters above thalweg.

Fig. 6. Box plot for microfibre concentration and sediment depth for all push-cores.

Fig. 7. Anthropogenic microparticle count with sediment depth for the push-cores located in Whittard Canyon. (A, B, D, and E) Location maps and high-resolution bathymetric maps of the Eastern Branch. 3X vertical exaggeration. (C and F) Anthropogenic microparticle trends for each push-core.

Fig. 8. Photographs taken of seabed push-core sampling from the Remotely Operated Vehicle. (A) Canyon thalweg at the upper-transect. (B) Canyon flanks at the upper-transect.

Fig. 9. Synthesis of microfiber transport and burial processes in submarine canyons. (A-D) Transport processes. (E) Sub-seafloor processes. (F) Anthropogenic forces.

**References**

Amaro, T., Huvenne, V.A.I., Allcock, A.L., Aslam, T., Davies, J.S., Danovaro, R., De Stigter, H.C., Duineveld, G.C.A., Gambi, C., Gooday, A.J., Gunton, L.M., Hall, R., Howell, K.L., Ingels, J., Kiriakoulakis, K., Kershaw, C.E., Lavaleye, M.S.S., Robert, K., Stewart, H., Van

Rooij, D., White, M., Wilson, A.M., 2016. The Whittard Canyon – A case study of submarine canyon processes. Progress in Oceanography146, 38-57.

Andrady, A.L., 2011, Microplastics in the marine environment. Marine Pollution Bulletin 62, 1596-1605.

Athey, S.N., Erdle, L.M., 2022. Are we underestimating Anthropogenic microfibre pollution? A critical review of occurrence, methods, and reporting. Environmental Toxicology and Chemistry 41, 822-837.

Bailey, L.P., Clare, M.A., Hunt, J.E., Kane, I.A., Miramontes, E., Fonnesu, M., Argiolas, R., Malgesini, G., Wallerand, R., 2024. Highly variable deep-sea currents over tidal and seasonal timescales. Nature Geoscience 17, 787-794.

Belzagui, F., Buscio, V., Gutiérrez-Bouzán, C., Vilaseca, M., 2021. Cigarette butts as a microfibre source with microplastic level of concern. Science of the Total Environment 762, e144165.

Brandon, J.A., Jones, W., Ohman, M.D., 2019. Multidecadal increase in plastic particles on coastal ocean sediments. Science Advances 5, eaax0587.

Browne, M.A.,Crump, P., Niven, S.J., Teuten, E., Tonkin, A., Galloway, T., 2011. Accumulation of microplastic on shorelines worldwide: sources and sinks. Environmental Science and Technology 45, 9175-9179.

Chen, M., Du, M., Jin, A., Chen, S., Dasgupta, S., Li, J., Xu, H., Ta, K., Peng, X., 2020. Forty-year pollution history of microplastics in the largest marginal sea of the western Pacific. Geochemical Perspective Letters 13, 42-47.

Choy, C.A., Robison, B.H., Gagne, T.O., Erwin, B., Firl, E., Halden, R.U., Hamilton, J.A., Katija, K., Lisin, S.E., Rolsky, C., Van Houtan, K.S., 2019. The vertical distribution and biological transport of marine microplastics across the epipelagic and mesopelagic water column. Science Advances 9, e7843.

Claessens, M., De Meester, S., Van Lunduyt, L., De Clerck, K., Janssen, C.R., 2011. Occurrence and distribution of microplastics in marine sediments along the Belgian coast. Marine Pollution Bulletin 62, 2199-2204.

Coppock, R.L., Cole, M., Lindeque, P.K., Queirós, A.M., Galloway, T.S., 2017. A small-scale portable method for extracting microplastics from marine sediments. Environmental Pollution 230, 829-837.

Courtene-Jones, W., Quinn, B., Ewins, C., Gary, S.F., Narayanaswamy, B.E., 2020. Microplastic accumulation in deep-sea sediments from the Rockall Trough. Marine Pollution Bulletin 154, e111092.

Curray, J., Moore, D.G., 1971. Growth of the Bengal Deep-Sea Fan and Denudation in the Himalayas. Geological Society of America Bulletin 87, 563-572.

Daly, E., Johnson, M.P., Wilson,A.M., Gerritsen, H.D., Kirakoulakis, K., Allcock, A.L., White, M., 2018. Bottom trawling at Whittard Canyon: Evidence for seabed modification, trawl plumes and food source heterogeneity. Progress in Oceanography 169, 227-240.

Dekiff, J.H., Klasmeier, J., Fries, E., 2014. Occurence and spatial distribution of microplastics in sediments from Norderney. Environmental Pollution 186, 248-256.

de Witte, B., Devriese, L., Bekaert, K., Hoffman, S., Vandermeersch, G., Cooreman, K., Robbens, J., 2014. Quality assessment of the blue mussel (Mytilus edulis): comparison between commercial and wild types. Marine Pollution Bulletin 85, 145-155.

Dimante-Deimantovica. I., Saarni, S., Barone, M., Buhhalko, N., Stivrins, N., Suhareva. N., Tylmann, W., Vianello. A., Vollertson, J., 2024. Downward migrating microplastics in lake sediments are a tricky indicator for the onset of the Anthropocene. Science Advances 10, eadi8136.

Duineveld, G., Lavaleye, M., Berghuis, E.M., de Wilde, P., 2011. Activity and composition of the benthic fauna in the Whittard Canyon and the adjacent continental slope (NE Atlantic). Oceanological Acta 24, 69-83.

Eggenhuisen, J.T., McCaffrey, W.D., 2012. Dynamic deviation of fluid pressure from hydrostatic pressure in turbidity currents. Geology 40, 295-298.

Fernandez-Arcaya, U., Ramirez-Llodra, E., Aguzzi, J., Allcock, A.L., Davies, J.S., Dissanayake, A., Harris, P., Howell, K., Huvenee, V.A.I., Macmillan-Lawler, M., Martin, J., Menot, L., Nizinski. M., Puig, P., Rowden, A.A., Sanchez, F., Van Den Beld, I.M.J., 2017. Ecological role of submarine canyons and need for canyon conservation: A review. Frontiers in Marine Science 4, e00005.

Finnegan, M.D., Süsserott, R., Gabbott, S.E., Gouramanis, C., 2022. Man-made natural and regenerated cellulosic fibres greatly outnumber microplastic fibres in the atmosphere. Environmental Pollution 310, e119808.

Frei, S., Piehl, S., Gilfedder, B.S., Löder, M.G.L., Krutzke, J., Wilhelm, L., Laforsch, C., 2019. Occurrence of microplastics in the hyporheic zone of rivers. Scientific Reports 9, e15256.

Global Fishing Watch, 2024. https://globalfishingwatch.org/map/index?start=2024-05-30T00%3A00%3A00.000Z&end=2024-08-30T00%3A00%3A00.000Z&longitude=26&latitude=19&zoom=1.49 (April 25th 2024).

Hage, S., Baker, M.L., Babonneau, N., Soulet, G., Dennielou, B., Silva Jacinto, R., Hilton, R.G., Galy, V., Baudin, F., Rabouille, C., Vic, C., Sahin, S., Açikalin, S., Talling, P.J., 2024. How is particulate organic carbon transported through the river-fed submarine Congo Canyon to the deep sea? Biogeosciences 21, 4251-4272.

Hall, R.A., Aslam, T. Huvenne, V.A., 2017. Partly standing internal tides in a dendritic submarine canyon observed by an ocean glider. Deep Sea Research Part I: Oceanographic Research Papers 126, 73-84.

Harris, P.T., Whiteway, T., 2011. Global distribution of large submarine canyons: Geomorphic differences between active and passive continental margins. Marine Geology 285, 69-86.

Heijnen, M.S., Mienis, F., Gates, A.R., Bett, B.J., Hall, R.A., Hunt, E., Kane, I.A., Pebody, C., Huvenne, V.A.I., Soutter, E.L., Clare, M.A., 2022. Challenging the highstand-dormant paradigm for land-detached submarine canyons. Nature Communications 13, e3448.

Jambeck, J.R., Geyer, R., Wilcox, C., Siegler, T.R., Perryman, M., Andrady, A., Narayan, R., Law, K.L., 2015. Plastic waste inputs from land into the ocean: Marine Pollution 347, 768-771.

Jiang, N., Chang, X., Huang, W., Khan, F.U., Fang, J.K-H., Hu, M., Xu, E.G., Wang, Y., 2024. Physiological response of mussel to rayon microfibres and PCB's exposure: Overlooked semi-synthetic micropollutant. Journal of Hazardous Materials 470, e134107.

Kane, I.A., Clare, M.A., 2019. Dispersion, accumulation, and the ultimate fate of microplastics in deep-marine environments: A review and future direction. Frontiers of Earth Science 7, e80.

Kane, I.A., Clare, M.A., Miramontes, E., Wogelius, R., Rothwell, J.R., Garreau., Pohl, F., 2022. Seafloor microplastic hotspots controlled by deep-sea circulation. Science 368, 1140-1145.

Koelmans, A., Kooi, M., Law, K.L., van Sebille, E., 2017. All is not lost: Deriving a top-down mass budget of plastic at sea. Environmental Research Letters 12, e114028.

Lebreton, L.C.M., van der Zwet, J., Damsteeg, J-W., Slat, B., Andrady, A., Reisser, J., 2017. River plastic emissions to the world's oceans. Nature Communications 8, e15611.

Li, M.Z., Prescott, R.H., Robertson, A.G., 2019. Observations of internal tides and sediment transport processes at the head of the Logan Canyon on central Scotian Slope, eastern Canada. Journal of Marine Systems 193, 103-125.

Maier, K.L., Rosenberger, K.J., Paull, C.K., Gwiazda, R., Gales, J., Lorenson, T., Barry, J.P., Talling, P.J., McGann, M., Xu, J. Lundsten, E., 2019. Sediment and organic carbon transport and deposition driven by internal tides along Monterey Canyon, offshore California. Deep Sea Research Part I: Oceanographic Research Papers 153, e103108.

Näkki, P., Setälä, O., Lehtiniemi, M., 2017. Bioturbation transports secondary microplastics to deeper layers in soft marine sediment in the northern Baltic Sea. Marine Pollution Bulletin 119, 255-261.

Napper, I.E., Thompson, R.C., 2016. Release of synthetic microplastic plastic fibres from domestic washing machines: Effects of fabric type and washing conditions. Marine Pollution Bulletin 112, 39-45.

Nel, H., Krause, S., Sambrook Smith, G.H., Lynch, I., 2019. Simple yet effective modification to the operation of the Sediment Isolation Microplastic unit to avoid polyvinyl chloride (PVC) contamination. MethodsX 6, 2656-2661.

Normandeau. A., Dafoe, L.T., Li, M.Z., Campbell, D.C., Jenner, K.A., 2024, Sedimentary record of bottom currents and internal tides in a modern highstand submarine canyon head, Sedimentology 71, 1061-1083.

Normark, W., 1970. Growth patterns of deep-sea fans. The American Association of Petroleum Geologists Bulletin 54, 2170-2195.

Palanques, A., Puig, P., Martín, J., Durán, R., Cabrera, C., Paradis, S., 2024. Direct and deferred sediment-transport events and seafloor disturbance induced by trawling in submarine canyons. Science of The Total Environment 947, e174470.

Paull, C.K., Green, H.G., Ussler, W., Mitts, P.J., 2002. Pesticides as tracers of sediment transport through Monterey Canyon. Geo-Marine Letters 22, 121-126.

Pierdomenico, M, Berhardt, A., Eggenhuisen, J.T., Clare, M.A., Lo Iacono, C., Casalbore, D., Davies, J.S., Kane, I., Huvenne, V.A.I., Harris, P.T., 2023. Transport and accumulation of litter in submarine canyons: a geoscience perspective. Frontiers in Marine Science 10, e101224859.

PlasticsEurope, 2023: Plastics – the fast Facts 2023. https://plasticseurope.org/knowledge-hub/plastics-the-fast-facts-2023/. (June 24th 2024).

Pohl, F., Eggenhuisen, J.T., Kane, I.A., Clare, M.A., 2020. Transport and burial of microplastics in deep-marine sediments by turbidity currents. Environmental Science and Technology 54, 4180-4189.

Rohais, S., Armitage, J.J., Romero-Sarmiento, M-F., Pierson, J-L., Teles, V., Bauer, D., Cassar, C., Sebag, D., Klopffer, M-H., Pelerin, M., 2024. A source-to-sink perspective of an anthropogenic marker: A first assessment of microplastic concentration, pathways, and accumulation across the environment. Earth-Science Reviews 254, e104822.

Talling, P.J., Cartigny, M.J.B., Pope, E., Baker, M., Clare, M.A., Heijnen, M., Hage, S., Parsons, D.R., Simmons, S.M., Paull, C.K., Gwiazda, R., Lintern, G., Hughes Clarke, J.E., Xu, J., Silva Jacinto, R. Maier, K.L., 2023. Detailed monitoring reveals the nature of submarine turbidity currents. Nature Reviews Earth and Environment 4, 642-658.

Tarhan, L.G., Droser, M.L., Planavsky, N.J., Johnston, D.T., 2015. Protracted development of bioturbation through the early Paleozoic Era. Nature Geoscience 8, 865-869.

Thompson, R.C., Olsen, Y., Mitchell, R.P., Davis, A., Rowland, S.J., 2004. Lost at Sea: Where is All the Plastic? Science 304, e838.

Treignier, C., Derenne, S., Saliot, A., 2006. Terrestrial and marine n-alcohol inputs and degradation processes relating to a sudden turbidity current in the Zaire canyon. Organic Geochemistry 37, 1170–1184.

Uddin, S., Fowler, S.W., Uddin, M.F., Behbehani, M., Naji, A., 2021. A review of microplastic distribution in sediment profiles. Marine Pollution Bulletin 163, e111973.

Van Cauwenberghe, L., Devriese, L., Galgani, F., Robbens, J., Janssen, C.R., 2015. Microplastics in sediments: a review of techniques, occurrence and effects. Marine Environmental Research 111, 5-17.

Van Cauwenberghe, L., Vanreusel, A., Mees, J., Janssen, C.R., 2013. Microplastic pollution in deep-sea sediments. Environmental Pollution 182, 495-499.

van Haren, H., F. Mienis., G. Duineveld., 2022. Contrasting internal tide turbulence in a tributary of the Whittard Canyon. Continental Shelf Research 236, e104679.

Vianello, A., Boldrin, A., Guerriero, P., Moschino, V., Rella, R., Sturaro, A., 2013. Microplastic particles in sediments of Lagoon of Venice, Italy: first observations on occurence, spatial patterns and identification. Estuarine, Coastal and Shelf Science 130, 54-61.

Waldschläger, K., Schüttrumpf, H., 2020. Infiltration behavior of microplastic particles with different densities, sizes, and shapes – from glass spheres to natural sediments. Environmental Science and Technology 54, 9366-9373.

Woodall, L.C., Sanchez-Vidal, A., Canals, M., Patterson, G.L.J., Coppock, R., Sleight, V., Calafat, A., Rogers, A.D., Narayanaswamy. B.E., Thompson, R.C., 2014. The deep sea is a major sink for microplastic debris. Royal Society Open Science 1, e140317.

Xue, B., Zhang, L., Li, R., Wang, Y., Guo, J., Yu, K., Wang, S., 2020. Underestimated microplastic pollution derived from fishery activities and "hidden" in deep sediment. Environmental Science and Technology 54, 2210-2217.

Zhang, X., Liu, Z., Li, D., Zhao, Y., Zhang, Y., 2024. Turbidity currents regulate the transport and settling of microplastics in a deep-sea submarine canyon. Geology 52, 646-650.

Zhong, G., Peng, X., 2021. Transport and accumulation of plastic litter in submarine canyons—The role of gravity flows. Geology 49, 581-586.

Zitko, V., Hanlon, M., 1991. Another source of pollution by plastics: Skin cleaners with plastic scrubbers. Marine Pollution Bulletin 22, 41-42.

## Supplemental Material

## Setting and Methods

### *Bathymetric Data*

The bathymetry of the Northeast Atlantic Ocean is derived from the Esri Ocean Basemap (https://www.arcgis.com/apps/mapviewer/index.html?webmap=67ab7f7c535c4687b6518e6d2343e8a2). The Digital Terrain Model data for the Whittard Canyon is based on the 2020 EMODnet digital terrain model (DTM) (https://doi.org/10.12770/bb6a87dd-e579-4036-abe1-e649cea9881a), which has a resolution of 1/16 x 1/16 arc minute of longitude and latitude (ca. 115 x 115 meters). The bathymetry for the Eastern Branch of Whittard Canyon is derived from the GEBCO_2023 Grid, GEBCO Compilation Group (2023) GEBO 2023 Grid (doi:10.5285/f98b053b-0cbc-6c23-e053-6c86abc0af7b). All the bathymetry data are analysed using ArcGIS Pro software to mark the moorings and sample locations, and to construct the longitudinal profiles and the cross-sections of the canyons.

### *Fishing Activity on the Celtic Margin*

Fishing activity data were downloaded from Global Fishing Watch (GlobalFishingWatch, 2024) and formatted in estimated annual fishing effort (in hours) per 0.01 x 0.01° grids. The fishing activities that disturb the seafloor were extracted.

## Laboratory Procedures

### *Fourier Transform Infrared Spectroscopy*

The analytical region was positioned over the identified particle, the particle was imaged, and then scanned over a spectrum range of 4000-650 $cm^{-1}$, with a resolution of 4 $cm^{-1}$ at a rate of 16 scans per analysis. The acquired spectra produced from the analysed particles were then processed and compared using the PerkinElmer Spectrum IR software with a standard reference library to assign polymer type.

***Grain-size Analysis***

The FLOWSYNC particle sizer uses tri-laser diffraction to measure particle size distribution with a lower particle limit size of 0.01 $\mu$m. The samples were subjected to a small amount of ultrasonic dispersion. Three aliquots were analysed to ensure that each sample was completely dispersed.

***$^{210}$Pb Sediment Accumulation Rates***

The sediment profiles of $^{210}$Pb are determined by alpha-spectrometry from $^{210}$Po. $^{210}$Pb is a naturally occurring radionuclide, part of the $^{238}$U decay series, with a half-life of 22.3 years. $^{210}$Po is extracted from the sediment by leaching with concentrated HCl or by total digestion using $HNO_3$ and HF. The $^{210}$Po is collected and counted with an alpha detector and the $^{210}$Pb profiles are plotted on a cumulative mass scale with an exponential curve. Where the $^{210}$Pb profiles deviate from the exponential curve, it is prudent to apply a conventional one-dimensional, two-layer vertical eddy diffusion model (following Carpenter *et al*. (1982)). The model assumes: 1) a constant rate of $^{210}$Pb supply (Appleby and Oldfield, 1978) and 2) a constant initial sedimentation rate (Krishnaswarmy *et al.*, 1971). A change in the gradient of the exponential curve may be due to sediment mixing processes in the sediment mixed layer, as is observed in BC64 and BC65, however this is accounted for in the model (Carpenter *et al*., 1982). The sandier intervals of the box-cores hold a lower $^{210}$Pb signature, so they were either avoided in the sub-sampling of the core horizons or sieved below 64 $\mu$m.

Table S1. Sample information, gravel%, sand%, silt%, and clay%, and scaled-up anthropogenic microparticle counts/50 g dry sediment. The associated coordinate projection for the location of the push-cores in WGS8.

| Sample number | Location | | Water depth (m) | Height above thalweg (m) | Core depth horizon (cm) | Gravel (%) | Sand (%) | Silt (%) | Clay (%) | Microfibre count (/ 50 g dry sediment) | Microplastic fragment count (/ 50 g dry sediment) | Microbead count (/ 50 g dry sediment) |
|---|---|---|---|---|---|---|---|---|---|---|---|---|
| | Lat (°N) | Long (°W) | | | | | | | | | | |
| PSH_060 | | | | | | | | | | | | |
| PSH_060_A | 48.61365 | -10.01576667 | 1546 | 34 | 0-1 | 0 | 99.62 | 0.38 | 0 | 4 | 0 | 0 |
| PSH_060_B | 48.61365 | -10.01576667 | 1546 | 34 | 1-2 | 1.1 | 98.90 | 0 | 0 | 10 | 8 | 0 |
| PSH_060_C | 48.61365 | -10.01576667 | 1546 | 34 | 2-3 | 14.07 | 85.93 | 0 | 0 | 17 | 3 | 0 |
| PSH_060_D | 48.61365 | -10.01576667 | 1546 | 34 | 3-4 | 10.16 | 89.84 | 0 | 0 | 21 | 0 | 0 |
| PSH_060_E | 48.61365 | -10.01576667 | 1546 | 34 | 4-5 | 22.90 | 77.09 | 0 | 0 | 30 | 0 | 0 |
| PSH_062 | | | | | | | | | | | | |
| PSH_062_A | 48.63688333 | -10.02356667 | 1360 | 220 | 0-1 | 0 | 64.34 | 35.66 | 0 | 14 | 0 | 0 |
| PSH_062_B | 48.63688333 | -10.02356667 | 1360 | 220 | 1-2 | 0 | 56.27 | 42.21 | 1.53 | 18 | 0 | 0 |
| PSH_062_C | 48.63688333 | -10.02356667 | 1360 | 220 | 2-3 | 0 | 52.14 | 44.91 | 2.95 | 11 | 0 | 0 |
| PSH_062_D | 48.63688333 | -10.02356667 | 1360 | 220 | 3-4 | 0 | 53.48 | 43.45 | 3.08 | 3 | 0 | 0 |
| PSH_062_E | 48.63688333 | -10.02356667 | 1360 | 220 | 4-5 | 0 | 56.03 | 40.29 | 3.68 | 10 | 0 | 0 |
| PSH_062_F | 48.63688333 | -10.02356667 | 1360 | 220 | 5-6 | 0 | 54.46 | 42.13 | 3.43 | 0 | 0 | 0 |
| PSH_062_G | 48.63688333 | -10.02356667 | 1360 | 220 | 6-7 | 0 | 45.98 | 48.79 | 5.23 | 11 | 4 | 0 |
| PSH_062_H | 48.63688333 | -10.02356667 | 1360 | 220 | 7-8 | 0 | N/A | N/A | N/A | 6 | 0 | 0 |
| PSH_062_I | 48.63688333 | -10.02356667 | 1360 | 220 | 8-9 | 0 | 53.06 | 43.62 | 3.32 | 9 | 0 | 0 |
| PSH_062_J | 48.63688333 | -10.02356667 | 1360 | 220 | 9-10 | 0 | 64.34 | 37.09 | 4.17 | 0 | 0 | 0 |
| PSH_064 | | | | | | | | | | | | |
| PSH_064_A | 48.63600667 | -10.0248 | 1303 | 277 | 0-1 | 0 | 52.65 | 44.92 | 2.43 | 5 | 0 | 0 |
| PSH_064_B | 48.63600667 | -10.0248 | 1303 | 277 | 1-2 | 0 | 43.78 | 50.71 | 5.51 | 8 | 0 | 0 |
| PSH_064_C | 48.63600667 | -10.0248 | 1303 | 277 | 2-3 | 0 | 40.28 | 53.72 | 6 | 8 | 0 | 0 |
| PSH_064_D | 48.63600667 | -10.0248 | 1303 | 277 | 3-4 | 0 | 40.65 | 54.73 | 4.62 | 9 | 0 | 0 |
| PSH_064_E | 48.63600667 | -10.0248 | 1303 | 277 | 4-5 | 0 | 34.08 | 57.59 | 8.33 | 3 | 0 | 0 |
| PSH_064_H | 48.63600667 | -10.0248 | 1303 | 277 | 7-8 | 0 | 41.3 | 52.79 | 5.91 | 19 | 0 | 0 |
| PSH_064_I | 48.63600667 | -10.0248 | 1303 | 277 | 8-9 | 0 | 41.78 | 52.56 | 5.66 | 5 | 0 | 0 |
| PSH_064_J | 48.63600667 | -10.0248 | 1303 | 277 | 9-10 | 0 | 45.21 | 49.46 | 5.33 | 14 | 0 | 0 |
| PSH_066 | | | | | | | | | | | | |
| PSH_066_A | 48.63545167 | -10.00317333 | 1259 | 321 | 0-1 | 0 | 38.7 | 53.82 | 7.48 | 9 | 0 | 0 |
| PSH_066_B | 48.63545167 | -10.00317333 | 1259 | 321 | 1-2 | 0 | 55.43 | 41.67 | 2.9 | 10 | 0 | 0 |
| PSH_066_C | 48.63545167 | -10.00317333 | 1259 | 321 | 2-3 | 0 | 48.02 | 45.68 | 6.3 | 7 | 0 | 0 |
| PSH_066_D | 48.63545167 | -10.00317333 | 1259 | 321 | 3-4 | 0 | 40.51 | 50.72 | 8.77 | 7 | 0 | 0 |
| PSH_066_E | 48.63545167 | -10.00317333 | 1259 | 321 | 4-5 | 0 | 35.87 | 59.06 | 5.07 | 3 | 0 | 0 |
| PSH_066_F | 48.63545167 | -10.00317333 | 1259 | 321 | 5-6 | 0 | 31.22 | 61.79 | 6.99 | 0 | 0 | 0 |
| PSH_066_G | 48.63545167 | -10.00317333 | 1259 | 321 | 6-7 | 0 | 30.18 | 62.82 | 7 | 3 | 0 | 0 |
| PSH_066_H | 48.63545167 | -10.00317333 | 1259 | 321 | 7-8 | 0 | 40.33 | 54.23 | 5.44 | 0 | 0 | 0 |
| PSH_066_I | 48.63545167 | -10.00317333 | 1259 | 321 | 8-9 | 0 | 38.4 | 55.57 | 6.03 | 0 | 0 | 0 |
| PSH_066_J | 48.63545167 | -10.00317333 | 1259 | 321 | 9-10 | 0 | 40.72 | 53.65 | 5.63 | 0 | 0 | 0 |
| PSH_069 | | | | | | | | | | | | |
| PSH_069_A | 48.64316667 | -9.99879 | 1062 | 518 | 0-1 | 0 | 43.45 | 49.5 | 7.05 | 50 | 8 | 0 |
| PSH_069_B | 48.64316667 | -9.99879 | 1062 | 518 | 1-2 | 0 | 41.99 | 51.74 | 6.27 | 43 | 0 | 0 |
| PSH_069_C | 48.64316667 | -9.99879 | 1062 | 518 | 2-3 | 0 | 42.68 | 49.87 | 7.45 | 14 | 9 | 0 |
| PSH_069_D | 48.64316667 | -9.99879 | 1062 | 518 | 3-4 | 0 | 42.25 | 50.59 | 7.16 | 8 | 0 | 8 |
| PSH_069_E | 48.64316667 | -9.99879 | 1062 | 518 | 4-5 | 0 | 46.82 | 47.26 | 5.92 | 16 | 0 | 8 |
| PSH_069_F | 48.64316667 | -9.99879 | 1062 | 518 | 5-6 | 0 | 44.59 | 51.57 | 3.84 | 3 | 0 | 0 |
| PSH_069_G | 48.64316667 | -9.99879 | 1062 | 518 | 6-7 | 0 | 41.23 | 55.05 | 3.72 | 14 | 0 | 22 |
| PSH_069_H | 48.64316667 | -9.99879 | 1062 | 518 | 7-8 | 0 | 51.5 | 45.41 | 3.09 | 6 | 0 | 0 |
| PSH_069_I | 48.64316667 | -9.99879 | 1062 | 518 | 8-9 | 0 | 66.49 | 31.89 | 1.62 | 5 | 0 | 0 |
| PSH_069_J | 48.64316667 | -9.99879 | 1062 | 518 | 9-10 | 0 | 55.31 | 42.55 | 2.14 | 22 | 3 | 0 |
| PSH_108 | | | | | | | | | | | | |
| PSH_108_A | 48.375593 | -10.0446445 | 3152 | 52 | 0-1 | 0 | 32.59 | 61.27 | 6.14 | 0 | 0 | 0 |
| PSH_108_B | 48.375593 | -10.0446445 | 3152 | 52 | 1-2 | 0 | 25.37 | 67.79 | 6.84 | 9 | 0 | 0 |
| PSH_108_C | 48.375593 | -10.0446445 | 3152 | 52 | 2-3 | 0 | 35.47 | 59.21 | 5.32 | 13 | 0 | 0 |
| PSH_108_D | 48.375593 | -10.0446445 | 3152 | 52 | 3-4 | 0 | 66.15 | 31.8 | 2.05 | 15 | 4 | 0 |
| PSH_108_E | 48.375593 | -10.0446445 | 3152 | 52 | 4-5 | 0 | 71.59 | 27.57 | 0.84 | 10 | 0 | 0 |
| PSH_108_F | 48.375593 | -10.0446445 | 3152 | 52 | 5-6 | 0 | 65.16 | 33.22 | 1.62 | 4 | 0 | 0 |
| PSH_108_G | 48.375593 | -10.0446445 | 3152 | 52 | 6-7 | 0 | 71.01 | 27.91 | 1.08 | 3 | 0 | 0 |
| PSH_108_H | 48.375593 | -10.0446445 | 3152 | 52 | 7-8 | 0 | 82.14 | 17.86 | 0 | 0 | 0 | 0 |
| PSH_108_I | 48.375593 | -10.0446445 | 3152 | 52 | 8-9 | 0 | 97.33 | 2.67 | 0 | 11 | 0 | 0 |
| PSH_108_J | 48.375593 | -10.0446445 | 3152 | 52 | 9-10 | 0 | 67.89 | 30.26 | 1.85 | 3 | 0 | 0 |
| PSH_113 | | | | | | | | | | | | |
| PSH_113_A | 48.371195 | -10.03929667 | 3204 | 0 | 0-1 | 0 | 85.73 | 14.27 | 0 | 32 | 0 | 0 |
| PSH_113_B | 48.371195 | -10.03929667 | 3204 | 0 | 1-2 | 0 | 95.27 | 4.73 | 0 | 25 | 0 | 0 |
| PSH_113_C | 48.371195 | -10.03929667 | 3204 | 0 | 2-3 | 0 | 97.85 | 2.15 | 0 | 6 | 6 | 0 |
| PSH_113_D | 48.371195 | -10.03929667 | 3204 | 0 | 3-4 | 0 | 96.8 | 3.2 | 0 | 10 | 0 | 0 |
| PSH_113_E | 48.371195 | -10.03929667 | 3204 | 0 | 4-5 | 0 | 93.65 | 6.35 | 0 | 15 | 0 | 0 |
| PSH_113_F | 48.371195 | -10.03929667 | 3204 | 0 | 5-6 | 0 | 88.07 | 11.93 | 0 | 17 | 0 | 0 |
| PSH_113_G | 48.371195 | -10.03929667 | 3204 | 0 | 6-7 | 0 | 88.85 | 11.15 | 0 | 5 | 0 | 0 |
| PSH_113_H | 48.371195 | -10.03929667 | 3204 | 0 | 7-8 | 0 | 92.87 | 7.13 | 0 | 12 | 2 | 0 |
| PSH_114 | | | | | | | | | | | | |
| PSH_114_A | 48.36871667 | -10.03463333 | 2995 | 209 | 0-1 | 0 | 12.3 | 78.35 | 9.35 | 31 | 0 | 0 |
| PSH_114_B | 48.36871667 | -10.03463333 | 2995 | 209 | 1-2 | 0 | 12.43 | 74.21 | 13.36 | 18 | 12 | 0 |
| PSH_114_C | 48.36871667 | -10.03463333 | 2995 | 209 | 2-3 | 0 | 28.77 | 64.56 | 6.67 | 9 | 0 | 0 |
| PSH_114_D | 48.36871667 | -10.03463333 | 2995 | 209 | 3-4 | 0 | 25.7 | 65.67 | 8.63 | 5 | 0 | 0 |
| PSH_114_E | 48.36871667 | -10.03463333 | 2995 | 209 | 4-5 | 0 | 12.95 | 79.55 | 7.5 | 5 | 0 | 0 |
| PSH_114_F | 48.36871667 | -10.03463333 | 2995 | 209 | 5-6 | 0 | 19.08 | 70.48 | 10.44 | 13 | 0 | 0 |
| PSH_114_G | 48.36871667 | -10.03463333 | 2995 | 209 | 6-7 | 0 | 19.09 | 71.75 | 9.16 | 14 | 0 | 0 |
| PSH_114_H | 48.36871667 | -10.03463333 | 2995 | 209 | 7-8 | 0 | 14 | 73.86 | 12.14 | 5 | 0 | 0 |
| PSH_114_I | 48.36871667 | -10.03463333 | 2995 | 209 | 8-9 | 0 | 13.85 | 77.71 | 8.44 | 13 | 0 | 0 |
| PSH_114_J | 48.36871667 | -10.03463333 | 2995 | 209 | 9-10 | 0 | 14.16 | 73.39 | 12.45 | 11 | 0 | 0 |
| PSH_116 | | | | | | | | | | | | |
| PSH_116_A | 48.36326 | -10.03335333 | 2773 | 431 | 0-1 | 0 | 25.05 | 67.94 | 7.01 | 51 | 0 | 0 |
| PSH_116_B | 48.36326 | -10.03335333 | 2773 | 431 | 1-2 | 0 | 22.27 | 69.15 | 8.58 | 16 | 0 | 0 |
| PSH_116_C | 48.36326 | -10.03335333 | 2773 | 431 | 2-3 | 0 | 18.28 | 73.86 | 7.86 | 11 | 0 | 0 |
| PSH_116_D | 48.36326 | -10.03335333 | 2773 | 431 | 3-4 | 0 | 19.04 | 73.91 | 7.05 | 29 | 6 | 0 |
| PSH_116_E | 48.36326 | -10.03335333 | 2773 | 431 | 4-5 | 0 | 18.66 | 72.68 | 8.66 | 17 | 0 | 0 |
| PSH_116_F | 48.36326 | -10.03335333 | 2773 | 431 | 5-6 | 0 | 14.94 | 74.67 | 10.39 | 10 | 5 | 0 |

| | | | | | | | | | | | | |
|---|---|---|---|---|---|---|---|---|---|---|---|---|
| PSH_116_G | 48.36326 | -10.03335333 | 2773 | 431 | 6-7 | 0 | 12.04 | 69.94 | 18.02 | 0 | 0 | 0 |
| PSH_116_H | 48.36326 | -10.03335333 | 2773 | 431 | 7-8 | 0 | 12.29 | 71.76 | 15.95 | 11 | 0 | 0 |
| PSH_116_I | 48.36326 | -10.03335333 | 2773 | 431 | 8-9 | 0 | 10.2 | 75.46 | 14.34 | 0 | 0 | 0 |
| PSH_116_J | 48.36326 | -10.03335333 | 2773 | 431 | 9-10 | 0 | 11.76 | 75.44 | 12.8 | 10 | 0 | 0 |

Table S2. Contamination control procedural blank data for the "sample preparation" stage and the "microparticle identification" stage. n.d. corresponds to no data.

| Sample number | Sample preparation exposure time (s) | Microfibre count | Microparticle identification exposure time (s) | Microfibre count |
|---|---|---|---|---|
| PSH_060 | | | | |
| PSH_060_A | 429 | 3 | 1150 | 0 |
| PSH_060_B | 540 | 0 | 920 | 0 |
| PSH_060_C | 515 | 0 | 879 | 0 |
| PSH_060_D | 457 | 0 | 681 | 0 |
| PSH_060_E | 500 | 0 | 534 | 0 |
| PSH_062 | | | | |
| PSH_062_A | 492 | 1 | 689 | 0 |
| PSH_062_B | 525 | 0 | 748 | 0 |
| PSH_062_C | 483 | 0 | 503 | 0 |
| PSH_062_D | 471 | 0 | 597 | 0 |
| PSH_062_E | 531 | 0 | 834 | 0 |
| PSH_062_F | 436 | 0 | 412 | 0 |
| PSH_062_G | 388 | 0 | 456 | 0 |
| PSH_062_H | 540 | 0 | 478 | 0 |
| PSH_062_I | 433 | 0 | 502 | 0 |
| PSH_062_J | 420 | 0 | 330 | 0 |
| PSH_064 | | | | |
| PSH_064_A | 408 | 0 | 1347 | 1 |
| PSH_064_B | 403 | 0 | 810 | 0 |
| PSH_064_C | 414 | 1 | 712 | 0 |
| PSH_064_D | 451 | 0 | 629 | 0 |
| PSH_064_E | 439 | 0 | 1422 | 0 |
| PSH_064_H | 381 | 0 | 878 | 0 |
| PSH_064_I | 430 | 0 | 720 | 0 |
| PSH_064_J | 490 | 0 | 934 | 0 |
| PSH_066 | | | | |
| PSH_066_A | 470 | 0 | 701 | 0 |
| PSH_066_B | 467 | 0 | 645 | 0 |
| PSH_066_C | 483 | 0 | 522 | 1 |
| PSH_066_D | 1962 | 0 | 326 | 0 |
| PSH_066_E | 580 | 0 | 400 | 0 |
| PSH_066_F | 449 | 0 | 354 | 0 |
| PSH_066_G | 552 | 0 | 570 | 0 |
| PSH_066_H | 442 | 0 | 385 | 1 |
| PSH_066_I | 458 | 0 | 380 | 0 |
| PSH_066_J | 415 | 0 | 321 | 0 |
| PSH_069 | | | | |
| PSH_069_A | n.d. | 0 | n.d. | 0 |
| PSH_069_B | n.d. | 2 | n.d. | 0 |
| PSH_069_C | n.d. | 0 | n.d. | 0 |
| PSH_069_D | n.d. | 1 | n.d. | 0 |
| PSH_069_E | n.d. | 0 | n.d. | 0 |
| PSH_069_F | n.d. | 2 | n.d. | 1 |
| PSH_069_G | n.d. | 2 | n.d. | 0 |
| PSH_069_H | n.d. | 3 | n.d. | 0 |
| PSH_069_I | n.d. | 3 | n.d. | 1 |
| PSH_069_J | n.d. | 6 | n.d. | 0 |
| PSH_108 | | | | |
| PSH_108_A | 421 | 0 | 410 | 0 |
| PSH_108_B | 410 | 0 | 329 | 0 |
| PSH_108_C | 407 | 0 | 717 | 0 |
| PSH_108_D | 467 | 0 | 682 | 0 |
| PSH_108_E | 403 | 0 | 724 | 0 |
| PSH_108_F | 367 | 0 | 520 | 0 |
| PSH_108_G | 366 | 0 | 489 | 0 |
| PSH_108_H | 406 | 0 | 226 | 0 |
| PSH_108_I | 354 | 0 | 460 | 0 |
| PSH_108_J | 362 | 0 | 357 | 0 |
| PSH_113 | | | | |
| PSH_113_A | 410 | 0 | 837 | 0 |
| PSH_113_B | 435 | 0 | 869 | 0 |
| PSH_113_C | 391 | 0 | 708 | 0 |
| PSH_113_D | 399 | 0 | 725 | 0 |
| PSH_113_E | 530 | 0 | 713 | 1 |
| PSH_113_F | 406 | 0 | 442 | 1 |
| PSH_113_G | 448 | 4 | 772 | 0 |
| PSH_113_H | 429 | 0 | 729 | 0 |
| PSH_114 | | | | |
| PSH_114_A | 954 | 0 | 1208 | 0 |
| PSH_114_B | 1065 | 1 | 1408 | 1 |
| PSH_114_C | 716 | 0 | 528 | 0 |
| PSH_114_D | 883 | 0 | 482 | 0 |
| PSH_114_E | 839 | 0 | 467 | 0 |
| PSH_114_F | 600 | 0 | 816 | 0 |
| PSH_114_G | 865 | 0 | 962 | 0 |
| PSH_114_H | 595 | 0 | 548 | 0 |
| PSH_114_I | 543 | 0 | 651 | 0 |
| PSH_114_J | 565 | 0 | 605 | 0 |
| PSH_116 | | | | |
| PSH_116_A | 412 | 0 | 456 | 0 |
| PSH_116_B | 424 | 1 | 566 | 0 |
| PSH_116_C | 465 | 0 | 493 | 0 |

| | | | | |
|---|---|---|---|---|
| PSH_116_D | 515 | 1 | 635 | 0 |
| PSH_116_E | 451 | 0 | 607 | 0 |
| PSH_116_F | 516 | 0 | 469 | 0 |
| PSH_116_G | 520 | 0 | 556 | 0 |
| PSH_116_H | 443 | 0 | 433 | 0 |
| PSH_116_I | 434 | 0 | 396 | 0 |
| PSH_116_J | 493 | 0 | 370 | 0 |

Table S3. Sample number and corresponding microparticle types color obtained from optical microscopy, and composition obtained from FTIR analysis.

| Sample number | Microparticle type | Microparticle color | Microparticle composition |
|---|---|---|---|
| PSH_060_A | Fibre | Black | Rayon |
| PSH_060_E | Fibre | Black | Chlorinated Rubber |
| PSH_062_A | Fibre | Black | Chlorinated Rubber |
| PSH_062_I | Fibre | Black | Chlorinated Rubber |
| PSH_064_B | Fibre | Blue | Polyester |
| PSH_064_C | Fibre | Black | Plastic additive |
| PSH_069_B | Fibre | Black | Polyvinyl chloride |
| PSH_108_B | Fibre | Black | Synthetic resin |
| PSH_113_B | Fibre | Black | Polypropylene |
| PSH_114_I | Fibre | Black | Acrylic |
| PSH_114_I | Fibre | Black | Acrylic |
| PSH_114_J | Fibre | Black | Chlorinated Rubber |
| PSH_116_B | Fibre | Black | Polyvinyl chloride |

Table S4. $^{210}$Pb values used to calculate sediment accumulation rates for the four box-cores.

| Box-core number | Core depth horizon (cm) | $^{210}$Pb total (mBq g-1) | $^{210}$Pb total 1s error (mBq g-1) |
|---|---|---|---|
| BC64 | | | |
| | 0-0.5 | 261.27 | 12.50 |
| | 0.5-1 | 268.59 | 11.71 |
| | 1-1.5 | 259.18 | 11.62 |
| | 2-2.5 | 310.24 | 12.65 |
| | 3-4 | 224.54 | 9.82 |
| | 5-6 | 290.17 | 12.28 |
| | 7-8 | 285.75 | 12.30 |
| | 9-10 | 154.65 | 7.77 |
| | 11-12 | 51.92 | 2.21 |
| | 13-14 | 23.56 | 1.25 |
| | 15-16 | 19.02 | 1.10 |
| | 17-18 | 21.86 | 1.16 |
| BC65 | | | |
| | 0-0.5 | 522.64 | 11.90 |
| | 0.5-1 | 493.74 | 11.98 |
| | 1-1.5 | 431.94 | 10.07 |
| | 2-2.5 | 404.47 | 9.58 |
| | 3-4 | 413.64 | 9.02 |
| | 5-6 | 312.98 | 8.02 |
| | 9-10 | 284.93 | 7.19 |
| | 13-14 | 186.10 | 5.17 |
| | 17-18 | 110.57 | 3.21 |
| | 24-25 | 66.14 | 2.33 |
| | 31-32 | 28.84 | 1.20 |
| | 38-39 | 26.82 | 1.22 |
| BC72 | | | |
| | 0-0.5 | 153.47 | 4.03 |
| | 0.5-1 | 157.50 | 4.14 |
| | 1-1.5 | 146.69 | 3.81 |
| | 1.5-2 | 126.40 | 3.57 |
| | 2-2.5 | 110.25 | 3.05 |
| | 3-5 | 60.72 | 1.89 |
| | 5-6 | 43.46 | 1.50 |
| | 7-8 | 17.39 | 0.81 |
| | 9-10 | 10.38 | 0.85 |
| | 11-12 | 10.40 | 0.83 |
| | 13-14 | 11.56 | 0.91 |
| | 15-16 | 12.93 | 0.99 |
| BC73 | | | |
| | 0-0.5 | 654.01 | 26.95 |
| | 0.5-1 | 640.97 | 24.23 |
| | 1-1.5 | 612.71 | 25.47 |
| | 2-2.5 | 664.32 | 22.85 |
| | 3-4 | 410.35 | 16.89 |
| | 5-6 | 547.83 | 22.24 |
| | 7-8 | 264.64 | 11.14 |
| | 11-12 | 525.91 | 20.83 |
| | 15-16 | 231.96 | 6.95 |
| | 21-22 | 103.19 | 3.79 |
| | 27-28 | 319.65 | 9.35 |
| | 33-34 | 278.11 | 8.56 |

## References

Appleby, P.G., and Oldfield, F., 1978, The calculation of lead-210 dates assuming a constant rate of supply of unsupported $^{210}$Pb to the sediment: CATENA, v. 5, p. 1-8.

Carpenter, R., Peterson, M.L., and Bennett, J.T., 1982, $^{210}$Pb-derived sediment accumulation and mixing rates for the Washington continental slope: Marine Geology, v. 48, p. 135-164.

Global Fishing Watch, 2024. https://globalfishingwatch.org/map/index?start=2024-05-30T00%3A00%3A00.000Z&end=2024-08-30T00%3A00%3A00.000Z&longitude=26&latitude=19&zoom=1.49 (April 25th 2024).

Krishnaswamy, S., Lal, D., Martin, J.M., and Meybeck, M., 1971, Geochronology of lake sediments: Earth and Planetary Science Letters, v. 11, p. 407-414.